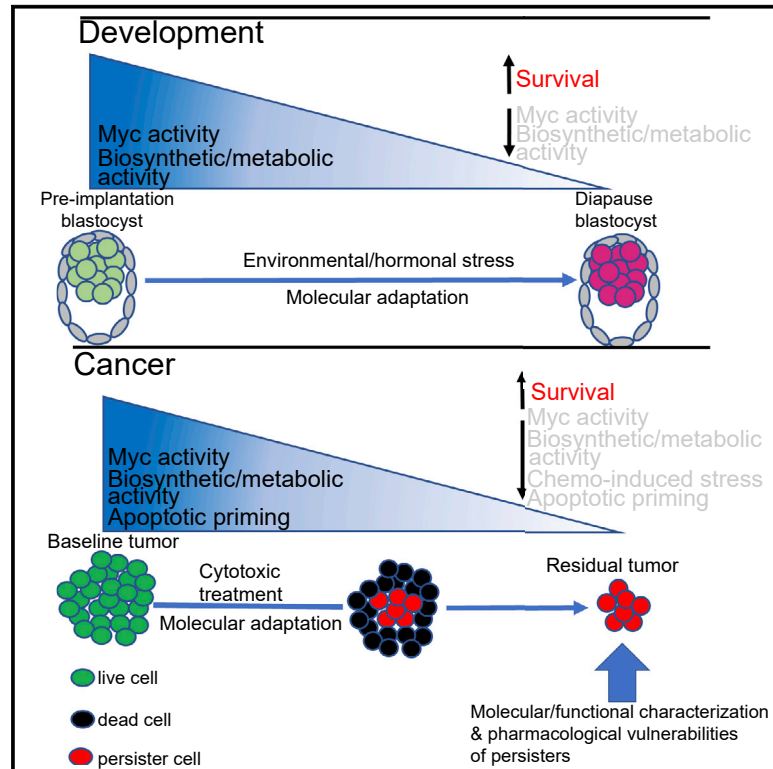


# Cancer Cell

## An Embryonic Diapause-like Adaptation with Suppressed Myc Activity Enables Tumor Treatment Persistence

### Graphical Abstract



### Authors

Eugen Dhimolea,  
Ricardo de Matos Simoes,  
Dhvanir Kansara, ..., Myles Brown,  
Aedin C. Culhane,  
Constantine S. Mitsiades

### Correspondence

eugen\_dhimolea@dfci.harvard.edu (E.D.),  
constantine\_mitsiades@  
dfci.harvard.edu (C.S.M.)

### In Brief

Dhimolea et al. document that cancer cell persistence during cytotoxic treatment is enabled by Myc inactivation and a biosynthetically paused adaptation resembling embryonic diapause. Myc-suppressed cancer cells have low redox stress and attenuated apoptotic priming. Interfering with this adaptive response of chemo-persistent cells enhances their chemosensitivity.

### Highlights

- 3D organoid cultures simulate the emergence of treatment-persistent residual tumors
- Chemo-persister cells have suppressed Myc and a diapause-like molecular adaptation
- Myc-suppressed cancer cells survive via reduced redox stress and apoptotic priming
- CDK9 inhibition reverts biosynthetic pause and enhances chemosensitivity

Article

# An Embryonic Diapause-like Adaptation with Suppressed Myc Activity Enables Tumor Treatment Persistence

Eugen Dhimolea,<sup>1,2,3,4,\*</sup> Ricardo de Matos Simoes,<sup>1,2,3,4</sup> Dhvanir Kansara,<sup>1,4</sup> Aziz Al'Khafaji,<sup>3</sup> Juliette Bouyssou,<sup>1,2,3</sup> Xiang Weng,<sup>1</sup> Shruti Sharma,<sup>1</sup> Joseline Raja,<sup>1</sup> Pallavi Awate,<sup>1</sup> Ryosuke Shirasaki,<sup>1,2,3,4</sup> Huihui Tang,<sup>1,2,3,4</sup> Brian J. Glassner,<sup>1,2,3,4</sup> Zhiyi Liu,<sup>5</sup> Dong Gao,<sup>6</sup> Jordan Bryan,<sup>3</sup> Samantha Bender,<sup>3</sup> Jennifer Roth,<sup>3</sup> Michal Scheffer,<sup>1,2,3,4</sup> Rinath Jeselsohn,<sup>1,2</sup> Nathanael S. Gray,<sup>1,2</sup> Irene Georgakoudi,<sup>5</sup> Francisca Vazquez,<sup>3</sup> Aviad Tsherniak,<sup>3</sup> Yu Chen,<sup>6</sup> Alana Welm,<sup>7</sup> Cihangir Duy,<sup>8,9</sup> Ari Melnick,<sup>8</sup> Boris Bartholdy,<sup>10</sup> Myles Brown,<sup>1,2</sup> Aedin C. Culhane,<sup>11</sup> and Constantine S. Mitsiades<sup>1,2,3,4,12,\*</sup>

<sup>1</sup>Department of Medical Oncology, Dana-Farber Cancer Institute Boston, MA, USA

<sup>2</sup>Harvard Medical School, Boston, MA, USA

<sup>3</sup>Broad Institute of MIT and Harvard, Cambridge, MA, USA

<sup>4</sup>Ludwig Center at Harvard, Boston, MA, USA

<sup>5</sup>Department of Biomedical Engineering, Tufts University, Medford, MA, USA

<sup>6</sup>Human Oncology and Pathogenesis Program, Memorial Sloan Kettering Cancer Center, New York, NY, USA

<sup>7</sup>Department of Oncological Sciences, Huntsman Cancer Institute, University of Utah, Salt Lake City, UT, USA

<sup>8</sup>Department of Medicine, Weill Cornell Medicine, New York, NY, USA

<sup>9</sup>Cancer Signaling and Epigenetics Program, Institute for Cancer Research, Cancer Epigenetics Institute, Fox Chase Cancer Center, Philadelphia, PA, USA

<sup>10</sup>Albert Einstein College of Medicine, Bronx, NY 10461, USA

<sup>11</sup>Department of Data Sciences, Dana-Farber Cancer Institute & Harvard T.H. Chan School of Public Health, Boston, MA, USA

<sup>12</sup>Lead Contact

\*Correspondence: [eugen\\_dhimolea@dfci.harvard.edu](mailto:eugen_dhimolea@dfci.harvard.edu) (E.D.), [constantine\\_mitsiades@dfci.harvard.edu](mailto:constantine_mitsiades@dfci.harvard.edu) (C.S.M.)

<https://doi.org/10.1016/j.ccell.2020.12.002>

## SUMMARY

Treatment-persistent residual tumors impede curative cancer therapy. To understand this cancer cell state we generated models of treatment persistence that simulate the residual tumors. We observe that treatment-persistent tumor cells in organoids, xenografts, and cancer patients adopt a distinct and reversible transcriptional program resembling that of embryonic diapause, a dormant stage of suspended development triggered by stress and associated with suppressed Myc activity and overall biosynthesis. In cancer cells, depleting Myc or inhibiting Brd4, a Myc transcriptional co-activator, attenuates drug cytotoxicity through a dormant diapause-like adaptation with reduced apoptotic priming. Conversely, inducible Myc upregulation enhances acute chemotherapeutic activity. Maintaining residual cells in dormancy after chemotherapy by inhibiting Myc activity or interfering with the diapause-like adaptation by inhibiting cyclin-dependent kinase 9 represent potential therapeutic strategies against chemotherapy-persistent tumor cells. Our study demonstrates that cancer co-opts a mechanism similar to diapause with adaptive inactivation of Myc to persist during treatment.

## INTRODUCTION

Many cytotoxic anti-cancer drugs, including those that can achieve clinical remission and prolong overall survival, often fail to completely eradicate cancers due to viable tumor fractions of variable sizes that persist throughout the treatment (“residual tumors”) and represent a reservoir for eventual relapse (Cortazar et al., 2014). The biological properties of drug-persistent tumor cells are incompletely understood, particularly for “non-targeted” cytotoxic therapeutics. Hundreds of molecular datasets exist for treatment-naïve or relapsed tumors, yet only a few

clinical studies (e.g., Kim et al., 2018; Kimbung et al., 2018; Magbanua et al., 2015) in breast cancer (BrCa) characterize treatment-persistent residual tumors via genome-scale molecular analyses of tumor samples obtained prior to, during, and/or at the end of neoadjuvant chemotherapy. Single-cell studies suggest that treatment-persistent residual cancer cells in patients may acquire a transcriptional program distinct from their respective pre-treatment tumors (Kim et al., 2018). Overall, the molecular profile of residual tumor cells, not just their detection as indicators of incomplete pathological response, has not been extensively used to stratify patients, predict clinical

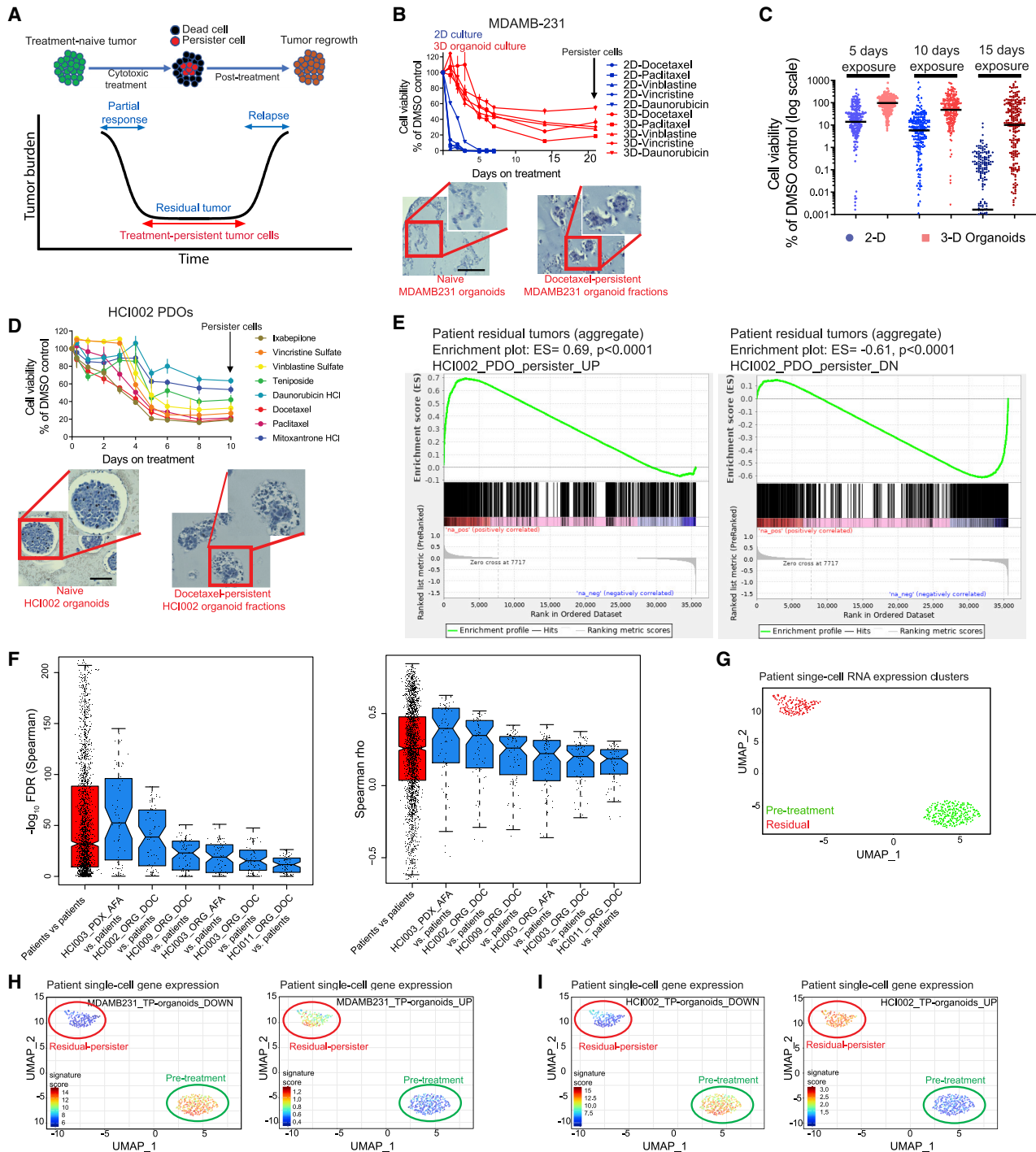


**Figure 1. Modeling Treatment-Persistent Residual Tumors in 3D Organoid Cultures**

(A) Schematic representation of treatment-persist residual tumor cells and their distinction from treatment-naive tumor cells or post-treatment tumors at the time of relapse.

(B) Longitudinal viability of MDAMB-231 3D organoids and 2D cultures (quadruplicates; mean  $\pm$  SEM) in the presence of the indicated cytotoxic drugs (100 nM) over time (top); plateauing of the viability curve indicates drug-persistent organoid fractions and respective control (bottom); scale bar, 100  $\mu$ m.

(C) Viability of 253 cancer cell lines (each transduced with its own DNA barcode distinct from the other cell lines of this panel; see STAR Methods) grown as 3D organoids or 2D cultures (triplicates) exposed to docetaxel (100 nM; three time points). Percentage of cell viability is shown in logarithmic scale; horizontal bars indicate median.

(legend continued on next page)

outcomes, or derive mechanisms governing the treatment-persistence phenotype. Furthermore, the mechanistic dissection of the chemo-persistent cancer cell state and the identification of its therapeutic vulnerabilities are hindered by the paucity of amenable *in vitro* models that simulate in a clinically relevant manner the phenotypic and molecular characteristics of the *in vivo* residual tumors.

Here, we used three-dimensional (3D) cultures and *in vivo* models to recapitulate the phenotype of residual disease in patients and elucidate the molecular properties of cancer cells that persist during cytotoxic treatment.

## RESULTS

### Pre-clinical Models of Treatment-Persistent Residual Tumors

Typical short-term (e.g., 24–72 h) *in vitro* assays do not necessarily simulate clinical responses to cytotoxic treatment, which are often incomplete, with variable residual tumor fractions persisting despite further drug administration (Figure 1A). We therefore longitudinally measured the viability of cancer cells during prolonged exposure to cytotoxic agents (including conventional chemotherapeutics) in 2D and 3D cultures. Herein we refer to 3D multicellular structures generated by cancer cell lines or patient-derived cells as “organoids.” In 2D cultures, clinically relevant doses of cytotoxic agents nearly eradicated the cancer cells within 4–6 days. In contrast, these same agents did not eliminate cancer cells in 3D organoids (even though they could readily penetrate these organoids; Figures S1A–S1C), but substantial fractions of most organoids remained viable for the duration of the experiment (Figure 1B). The fractions of treatment-persistent organoids (referred to henceforth as TP-organoids) after the initial drug-induced killing varied across drug classes, e.g., from ~20% to 50% in MDAMB-231 organoids. To assess the generalizability of this phenotype, we cultured under 2D and 3D conditions a pool of 253 cancer cell lines, each with its distinct DNA “barcode” (Yu et al., 2016). After 15 days of chemotherapy treatment, most cell lines in 3D cultures had >10% viability, but were reduced to <0.1% in 2D cultures (Figure 1C). To further evaluate the biological relevance of the drug persistence in 3D organoids, we developed and characterized several BrCa and prostate cancer (PrCa) patient-derived organoids (PDOs) and patient-derived xenograft (PDX) models (Figure S1D). Prolonged (up to 3 weeks) treatment of PDOs with chemotherapeutics and targeted agents did not eradicate all cancer cells,

but resulted in residual TP-organoids (indicated by the plateauing levels of the time-lapse viability curves; Figures 1D and S1E–S1G), reminiscent of clinical post-treatment residual disease in solid tumors. Notably, the respective drug-treated PDX models mirrored the longitudinal drug response in organoids (Figures S1E and S1F).

To assess at the molecular level the clinical relevance of our pre-clinical models, we used as reference the serial samples obtained from BrCa patients before versus during neoadjuvant chemotherapy administration from four clinical studies (Gonzalez-Angulo et al., 2012; Gruosso et al., 2016; Kim et al., 2018; Kimbung et al., 2018; Magbanua et al., 2015). The transcriptional changes in TP-organoid fractions (versus DMSO-treated organoids) and in residual PDX tumors (versus controls) correlated with those in residual BrCa tumors in patients after (versus before) neoadjuvant chemotherapy (Figures 1E, 1F, S1H, and S1I and Tables S1 and S2). In addition, the transcriptional profiles of TP-organoids resembled those of individual chemo-persistent residual tumor cells, but not pre-treatment cells, in patients (Figures 1G–1I). Thus, TP-organoid fractions *in vitro* reflect the molecular profiles of chemo-refractory residual tumors *in situ* in xenografts or in patients.

### Treatment Persistence Is Not Driven by Newly Acquired Mutations or Rare Pre-existing Clones

When tumor cells were isolated from treatment-naive 3D cultures, plated in 2D cultures, and exposed to cytotoxic agents, they lost their proneness for drug persistence (Figure S2A and S2B), indicating that the decreased drug sensitivity in 3D is not driven by resistant clones selectively expanded under these conditions. To determine whether the clonal compositions of TP-organoids versus pre-treatment controls are different, whole-exome sequencing was performed and revealed no significant change in their patterns of single-nucleotide variants after treatment *in vitro* (Figure 2A). In 3D cultures, where each organoid is generated from one single initial cell, TP-organoid fractions emerged from most or all organoids (Figures 1B, 1D, S1E, and S2C). This differs quantitatively and qualitatively from drug-tolerant persister (DTP) cells previously reported in 2D cultures (Hata et al., 2016; Sharma et al., 2010), which represent a small subset of rare cells (typically 0.01%–1% of cells), putatively resulting from pre-existing clones or rare stochastic epigenetic states (schematic in Figure S2D). Recasting TP-organoids harvested at the plateau phase (schematic in Figure S2E) in Matrigel, after drug washout, allowed for *de novo* generation of fully

(D) Longitudinal response of HCI-002 PDOs (quadruplicates; mean  $\pm$  SEM) to chemotherapeutic agents (100 nM); curve plateau indicates treatment-persister residual tumor cells (top). Representative H&E staining images of indicated organoids (bottom); scale bar, 100  $\mu$ m.

(E) Transcriptional changes in clinical residual tumors (versus respective baselines; aggregate of PROMIX trial patients) depicted as enrichment plots for genes upregulated (left) or downregulated (right) in HCI002 TP-organoids (similar results were obtained with other TP-organoid models).

(F) Gene-level pairwise comparisons of transcript changes in clinical chemotherapy-persistent residual BrCa tumors (PROMIX trial, after two chemotherapy cycles [Kimbung et al., 2018], dataset GEO: GSE87455) and our BrCa TP-organoid models (versus baseline): graphs depict the Spearman correlation FDR (left) and coefficient (right) values of pairwise comparisons between transcriptional changes in different sets of treatment-persistent tumor cells, namely: comparisons between each patient tumor versus all other patient tumors in this cohort (red) and between each patient tumor versus each of the BrCa TP-organoid/PDX models (blue) treated with docetaxel (DOC) or afatinib (AFA). The analysis was performed on the subset of 1,401 genes that were differentially expressed on the aggregate patients' residual tumors versus respective baseline (FDR  $\leq$  0.05) from limma t test analysis of the global two-group comparison.

(G–I) UMAP plot of single-cell RNA-sequencing profiles in baseline and chemo-persister residual triple-negative breast cancer (TNBC) patient tumor (G; separate clusters indicate newly acquired transcriptional profile in the residual cancer cells) and respective UMAP plots for expression in these single cells of the transcriptional signatures derived from docetaxel-persister organoids (versus respective controls) in TNBC 3D-culture models of MDAMB-231 (H) and HCI002 (I) cells.

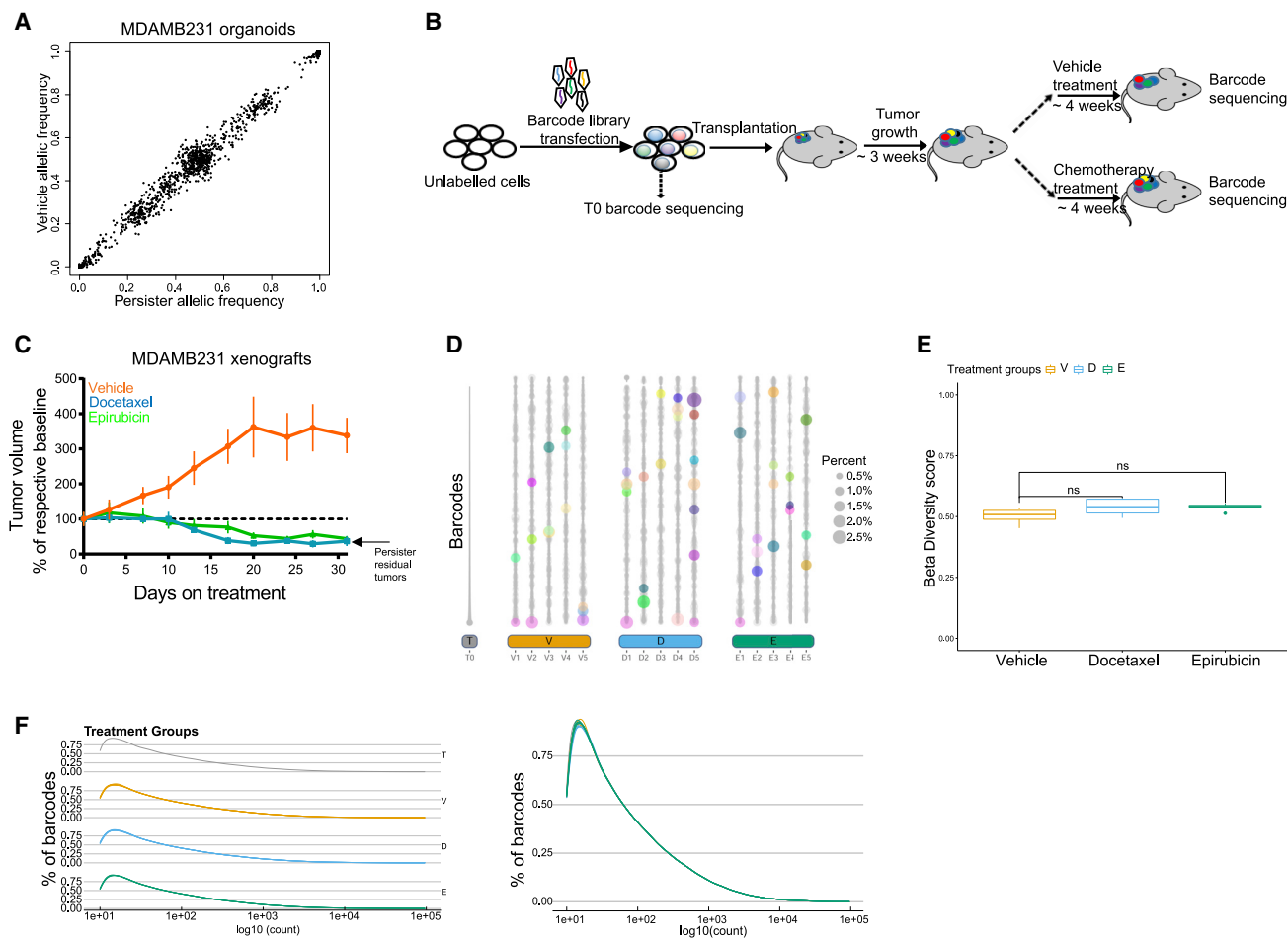


**Figure 2. Treatment Persistence in Pre-clinical Models Is Not Driven by Selection of *De Novo* Mutations or Rare Pre-existing Clones**

(A) Two-dimensional density plot of single-nucleotide variant allelic frequencies from whole-exome sequencing of docetaxel-persister versus treatment-naive 3D MDAMB-231 organoids.

(B) Schematic representation of the DNA barcode-based clonal tracking *in vivo* experiment.

(C) Treatment of MDAMB-231 barcoded xenografts induces tumor regression, which segues into treatment-persister residual tumors (mean  $\pm$  SEM).

(D) Barcode abundance in the tumor cell population prior to engraftment (T0, gray), and in tumors treated with DMSO vehicle control (V, orange), docetaxel (D, blue), or epirubicin (E, green). Barcodes are ordered vertically according to their initial abundance (lowest to highest from top to bottom) at T0, and barcodes with >1% abundance are assigned random colors.

(E) Beta diversity (Bray-Curtis) scores for the barcodes observed for tumors in each of the treatment groups.

(F) Barcode distribution in residual tumors and vehicle control, separately for each group (left) or superimposed (right).

grown organoids, similar to the original cultures, within variable time periods (ranging from 2 to 12 weeks depending on the type of drug and organoid; examples in Figures S2F and S2G). These *de novo* grown organoids had drug-sensitivity profiles similar to those of parental drug-naive cells (Figures S2H and S2I), further indicating that the observed drug persistence is not attributable to selection of constitutively drug-resistant clones.

To directly monitor at high resolution the clonal dynamics during the emergence of treatment-persister tumors *in vivo*, we used DNA-barcode-mediated clonal tracking approaches (details under STAR Methods). We transduced MDAMB-231 cells with a lentiviral library comprising  $\sim$ 50 million unique DNA barcodes at a low multiplicity of infection to ensure that most transduced cells received only one unique DNA barcode, and transplanted the

barcoded cells into immunocompromised mice (Figure 2B). After tumors reached  $\sim$ 50–100 mm<sup>3</sup>, mice were randomly assigned to receive chemotherapy, which induced tumor regression (Figure 2C) and establishment of residual tumors, or vehicle. Next-generation sequencing to quantify the DNA barcodes in harvested control xenografts indicated a major decrease in barcode library complexity during the tumor cell engraftment (with estimated engraftment rate of  $\sim$ 20%–30%) but no consistent enrichment of engrafted barcodes between replicates. Importantly, chemotherapy treatments did not enrich any barcode in residual tumors, as assessed by geometric mean test of ranks (Breitling et al., 2004) or by analysis of variance with false discovery rate (FDR) correction for multiple testing (Li et al., 2014), indicating that treatment persistence in the residual tumors was not driven by a specific pre-existing clone (Figure 2D). Beta diversity, an

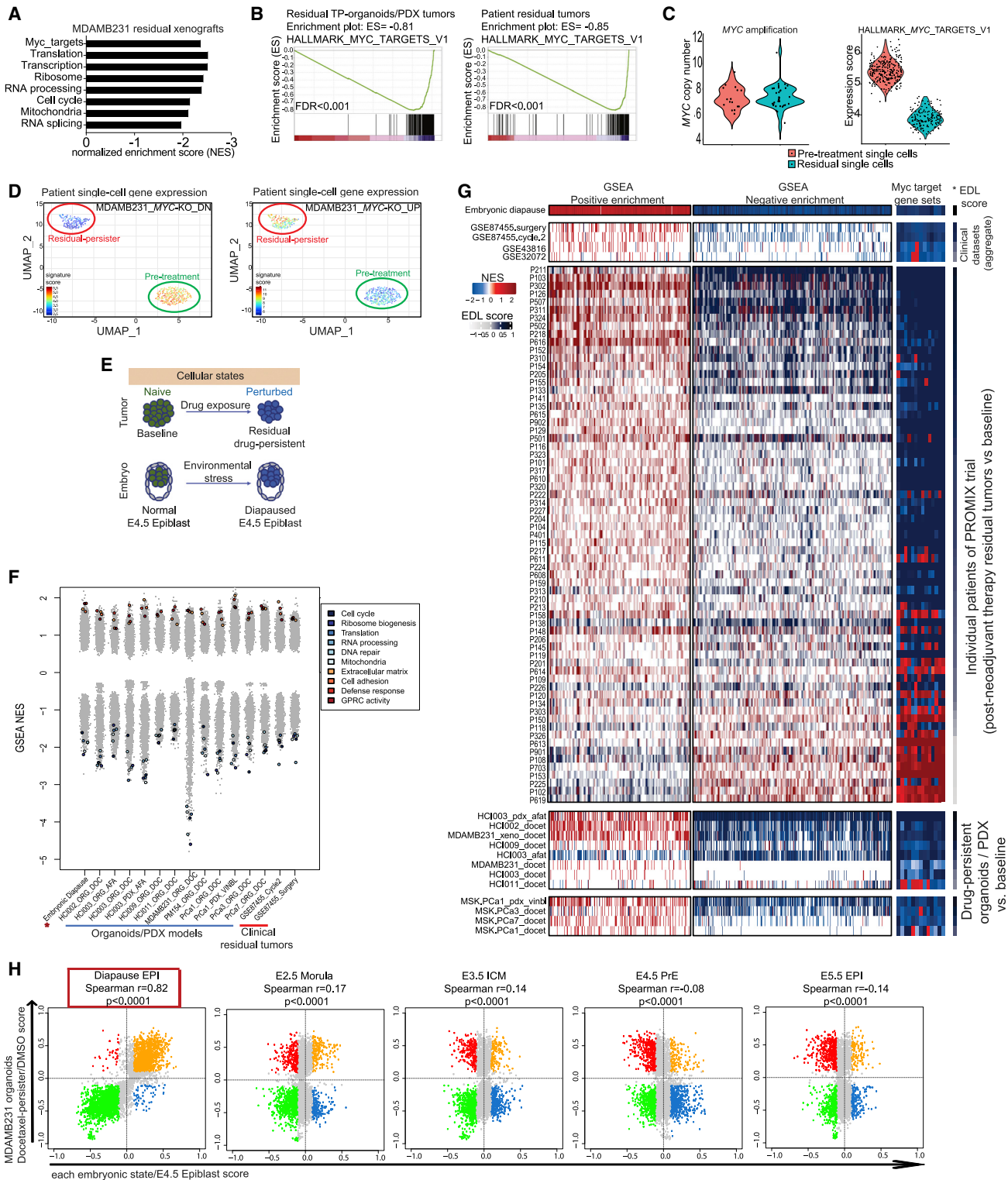


**Figure 3. The Transcriptional Adaptation in Treatment-Persistent Tumors Encompasses Suppression of Myc Activity and Mimics Embryonic Diapause**

(A) Examples of transcriptional signatures that are suppressed in docetaxel-persistent residual MDAMB-231 xenografts.

(B) Gene set enrichment analysis (GSEA) enrichment plots of Myc target genes in treatment-persistent residual tumor cells (compared with baseline) in pre-clinical models (left) and in clinical samples (right; PROMIX trial dataset GEO: GSE87455). Aggregate enrichment in organoid/PDX models or patient cohort is shown.

(C) Single-cell analysis of MYC gene copy number and transcriptional activity in baseline and chemo-persister residual cells of a TNBC patient (Kim et al., 2018).

(legend continued on next page)

index of compositional heterogeneity in the barcoded cell population, was not significantly altered in chemo-persistent residual tumors versus control (Figure 2E). Concordantly, the barcode frequency distribution (including high-abundance barcodes) was similar between cohorts (Figure 2F).

Together, these *in vivo* and *in vitro* observations indicate that persistence after acute cytotoxic treatment in these xenografts and 3D organoid models cannot be attributed to putative pre-existing cell populations or rare clones that either were *a priori* drug resistant or acquired constitutive resistance during treatment.

### The Transcriptional Adaptation in Treatment-Persistent Tumors Is Driven by Suppression of Myc Activity and Mimics Embryonic Diapause

As DNA barcoding and mutational analyses did not support a genetic mechanism for treatment persistence in our models, we examined the transcriptional profiles of chemo-persistent residual xenografts, organoids, and clinical (post-neoadjuvant chemotherapy) BrCa samples (Kimbung et al., 2018; Magbanua et al., 2015) to identify potential transcriptional adaptations that could account for this treatment persistence. Chemo-persistent residual tumor cells were predominantly characterized by a substantial suppression of transcripts related to cellular biosynthetic processes and the activity of transcription factor Myc (Figure 3A). We observed marked suppression of Myc transcriptional output across treatment-persistent residual tumors in patients and pre-clinical models (Figure 3B). In single-cell studies of BrCa patient tumor cells with MYC amplification at baseline, residual treatment-persistent cells maintained their MYC amplification but had suppressed Myc activity (Figure 3C). Myc protein together with biosynthetic markers was also downregulated during the emergence of TP-organoids (Figure S3A). Myc protein reduction preceded its mRNA downregulation (Figure S3B), indicating that Myc may be initially regulated post-transcriptionally during treatment-induced stress. We observed no consistent differences in the expression of molecules that could have contributed to suppression of Myc transcript or protein levels, including microRNAs (e.g., the let7-miRNA family) and known E3 ligases for c-Myc (e.g., Skp2, Fbw7, Huwe1) (data not shown).

Given that Myc is a master regulator of biosynthesis and metabolism in both normal and transformed cells, we asked whether inactivation of Myc in cancer cells suffices to induce the biosynthetically paused state that we observed in treatment-persistent residual tumors. We knocked out MYC in MDAMB-231 cells us-

ing CRISPR-mediated gene editing (Figure S3C) and observed strong suppression of the Myc transcriptional output (Figures S3D and S3E), suppressed biosynthetic activity (Figure S3F), and an overall transcriptional profile similar to that in single cancer cells of residual tumors (but not cells of pre-treatment tumors) in patients (Figure 3D).

Notably, a role for Myc suppression as an inducer of cellular adaptation into stress-resilient biosynthetic dormancy has also been previously reported in embryonic diapause, which is a reversible physiological state of suspended development in E4.5 epiblasts triggered by adverse conditions and has been molecularly characterized in recent studies (Boroviak et al., 2015; Scognamiglio et al., 2016) (Figures S3G and S3H and Table S3). We therefore compared molecular profiles of residual drug-resilient tumor fractions in organoids, PDX, and patients with that of diapaused mouse epiblast (Figure 3E). Processes related to metabolism (e.g., mitochondrial activity), regulation of gene expression (e.g., RNA processing, RNA splicing, RNA export from nucleus), protein synthesis (e.g., ribosome biogenesis, translation), and proliferation (e.g., DNA replication, replication fork, chromosome segregation) were strongly suppressed in all these biological settings, whereas processes related to extracellular matrix (ECM) reorganization (e.g., collagen modification) and cell adhesion (e.g., integrin binding) were commonly upregulated (Figure 3F). Similar to previous studies of embryonic diapause (Bulut-Karslioglu et al., 2016; Scognamiglio et al., 2016), we performed molecular analyses at gene-set and individual-gene levels. We found a strong positive correlation between the transcriptional changes in residual drug-persistent tumor fractions in our pre-clinical models and in most BrCa cases (versus their respective treatment-naïve states) and the transcriptional changes during the transition of the normal E4.5 epiblast to the diapaused epiblast stage, but not other embryonic stages (Figures 3G, 3H, S4A–S4E, S5A–S5E). The correlation scores of the embryonic diapause-like (henceforth referred to as EDL) molecular signatures of treatment-persistent residual cancer cells in our pre-clinical models, and most clinical samples are consistent with those of the *in vitro* mouse models of diapause (Bulut-Karslioglu et al., 2016; Scognamiglio et al., 2016). We compared the transcriptional profiles of BrCa tumors at baseline for patients whose residual tumors did versus did not acquire an EDL signature upon treatment; thus establishing an “EDL-proneness” signature of baseline tumors (which is a distinct metric from the EDL signature in residual tumors; see STAR Methods). Interestingly, and perhaps counterintuitively,

(D) UMAP plots of single-cell RNA profiles from baseline and residual patient tumor with MYC amplification, showing the expression patterns in individual cells of the transcriptional signature induced by CRISPR-Cas9-mediated editing of MYC in MDAMB-231 cells.

(E) Schematic representation of adaptive cellular states examined.

(F) GSEA results from comparisons of mouse embryonic diapause versus normal epiblast (Boroviak et al., 2015; Scognamiglio et al., 2016), drug-persistent patient tumors versus their respective pre-treatment baseline (Kimbung et al., 2018), and BrCa/PrCa TP-organoid (ORG) and PDX residual tumors after treatment with docetaxel (DOC), afatinib (AFA), or vinblastine (VINBL) versus their respective vehicle-treated samples. Normalized enrichment scores (NES) are shown.

(G) Heatmap depicting the MSigDB gene sets significantly (FDR <0.05) altered in embryonic diapause and their respective enrichment status in drug-persistent residual tumor fractions in examined patient datasets (aggregate expression), in individual BrCa patients from the PROMIX trial (GEO: GSE87455), and in our pre-clinical models; notice the association between the EDL score (see STAR Methods) and the suppression of Myc target gene sets (14 MSigDB gene sets with negative enrichment [FDR <0.05] in either embryonic diapause or the clinical dataset are shown). Similar analysis of the I-SPY trial is shown in Figure S5D.

(H) 2D GO pathway expression analyses (including CPDB pathways and GO terms; see STAR Methods) comparing docetaxel-persistent MDAMB-231 TP-organoids with different mouse embryo developmental stages (Boroviak et al., 2015). Spearman correlation coefficients indicate significant similarity of the TP-organoids to the diapaused E4.5 epiblast but not to other embryonic stages (comparisons similar to those performed by Bulut-Karslioglu et al., 2016, and Scognamiglio et al., 2016).

given the dormant profile of EDL cancer cells, in the METABRIC dataset, patients with EDL-prone baseline tumors had worse clinical outcomes (Figure S5F).

### Suppression of Myc in Tumor Cells Induces a Diapause-like State and Persistence to Cytotoxic Treatment

We asked whether Myc inactivation and the associated EDL signature in residual tumor cells are a consequence of the treatment or an enabler of drug persistence. To address this question, we functionally assessed the role of Myc on the chemosensitivity of cancer cells. CRISPR-based loss of function for *MYC* in cancer cells (Figure S3C) induced an EDL transcriptional signature (Figure 4A) and attenuated the effect of cytotoxic chemotherapy (Figures 4B–4D). Conversely, doxycycline-induced ectopic expression of Myc increased acute drug cytotoxicity and reduced the chemo-persistent fraction in 3D cancer organoids (Figures S6A–S6D). These results indicate that, similar to embryonic diapause, suppressed Myc activity in cancer cells enables survival under stress. Interestingly, baseline tumors of BrCa patients with *MYC* amplifications in the METABRIC dataset had higher EDL-proneness score (see STAR Methods for definition) compared with tumors without *MYC* amplification (Figure S6E), indicating that tumors with *MYC* amplification may be more likely to persist during treatment through an EDL state with suppressed Myc activity.

Given the recent emphasis on therapeutic strategies targeting Myc via inhibition of its transcriptional co-activator BET bromodomain-containing protein Brd4 (Delmore et al., 2011; Loven et al., 2013), we examined how the pharmacological suppression of Myc activity affects the acute chemotherapeutic cytotoxicity in cancer cells. The BET inhibitor JQ1 induced a Myc-suppressed EDL transcriptional profile (Figure S6F), attenuated the cytotoxic effect of chemotherapeutic agents in BrCa cell lines and PDOs (Figures 4E, 4F, and S6G–S6J), and partially abrogated the chemosensitization induced by Myc overexpression (Figure S6K). These results further support the functional role of Myc suppression in conferring drug-persistent dormancy in cancer cells. The abrogation of chemotherapeutic cytotoxicity by JQ1 was also confirmed in cell lines from hematological cancers (data not shown), indicating the generalizability of this mechanism across cancer types and drug classes.

### Suppression of Myc Activity Reduces Redox Stress and Attenuates Apoptotic Priming in Cancer Cells

Myc controls a multitude of cellular processes that directly or indirectly regulate cellular stress and cell death (Evan et al., 1992; McMahon, 2014; Meyer et al., 2006). Exposure to chemotherapeutic agents induced redox stress in treatment-naive organoids, but not in EDL TP-organoids (Figure 5A). Consistently, exposure to JQ1 also attenuated the chemotherapy-induced cellular redox stress in BrCa cells (Figure 5B) and phenocopied the effect of the redox stress-reducing agent N-acetylcysteine (Figure 5C). Overall, these findings are congruent with the proposed role of redox stress in chemotherapeutic cytotoxicity (Luo et al., 2009; Schumacker, 2006) and corroborate that suppression of Myc achieves dormant biosynthetic rates that contribute, at least in part, to survival in the presence of cytotoxic agents via mitigation of treatment-induced cellular stress in residual cancer cells.

Interestingly, when cells were exposed to H<sub>2</sub>O<sub>2</sub>, an exogenous source of stress in the form of free radicals, JQ1 could again attenuate H<sub>2</sub>O<sub>2</sub>-induced apoptosis and cell death (Figures 5D and 5E), suggesting that suppression of Myc activity may not only mitigate treatment-induced redox stress, but also increase the cellular apoptotic threshold in the presence of exogenously forced increase in redox stress. We examined Bcl-2 family members (Figure 5F) or antioxidant enzymes (data not shown) for potential transcript changes across chemo-persister TP-organoid and PDX tumors but did not observe a consistent pattern. We thus turned to functional testing of pro-apoptotic and anti-apoptotic Bcl-2 family proteins in the treatment-persister cells. TP-organoids did not exhibit increased sensitivity to inhibition of Bcl-2 (Figure 5G) or Mcl-1 (not shown). Antioxidant N-acetylcysteine or JQ1 did not cause major change in the response of chemotherapy-naive tumor cells to Bcl-2 inhibition (Figure 5H). Together, these data suggest that upregulation or activation of these anti-apoptotic proteins is unlikely to be the main mediator of the effect of Myc suppression in the treatment-persister state. We next examined the function of pro-apoptotic BH3 family members in TP-organoids, using the BH3 profiling method (Montero et al., 2015): TP-organoids had reduced cytochrome c release (versus DMSO control) after exposure to pro-apoptotic peptides BIM and BID (Figure 5I), indicative of reduced apoptotic priming in chemo-persister cells. We generated BrCa cells expressing a doxycycline-inducible dCas9/KRAB system (Kearns et al., 2014) for CRISPR interference (CRISPRi), which allows controlled suppression of *MYC* transcription (Figure 5J). Suppression of *MYC* reduced cell sensitivity to exogenous BIM and BID peptides (Figure 5K). Concordantly, treatment of cells with JQ1 also attenuated the ability of BIM and BID to initiate apoptosis (Figure 5L). Together, these results indicate that Myc suppression in persister cells can attenuate apoptotic priming, which may also contribute to survival in the presence of cytotoxic agents.

### The Distinct and Reversible Features of the Diapause-like Persister Tumor Cell Adaptation

Similar to embryonic diapause, proliferative quiescence was not the sole molecular determinant of diapause-like treatment-persister cancer cells. Instead, these cells encompassed additional components in their core signature of diapause-like adaptation, including biosynthetic quiescence, suppression of redox stress, and upregulation of cell-ECM interaction-related modules (Figure 3F). Consequently, the transcriptional differences between TP-organoids versus treatment-naive counterparts were distinct from the differences between proliferatively quiescent versus cycling cells in 3D cultures (Figure S7A). Furthermore, the JQ1-mediated chemo-persistence effect was not phenocopied by *bona fide* cell cycle blockers such as the Cdk4/6 inhibitor abemaciclib or Aurora kinase inhibitor AMG900 (Figures S7B–S7H). Abemaciclib-treated organoids exhibited the molecular hallmarks of arrested cell cycle, including dephosphorylation of Rb and suppression of cell-cycle markers (Figures 6A–6D), but were not more chemo-resistant compared with abemaciclib-naive organoids (Figures 6E and 6F). Importantly, exposure of cell-cycle-arrested organoids (obtained by longitudinal treatment with abemaciclib) to chemotherapy generated chemo-persister fractions with suppressed Myc and

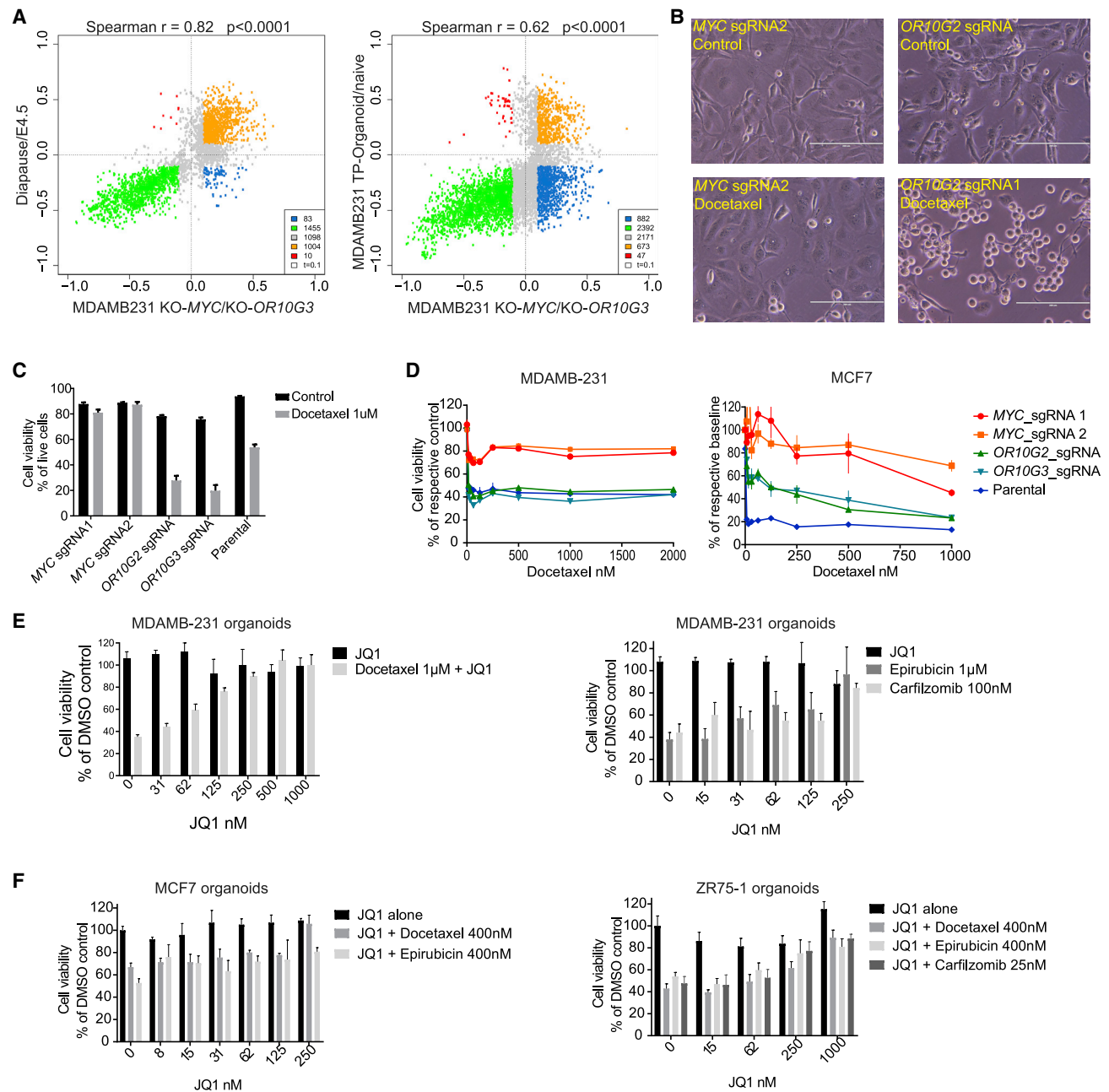


**Figure 4. Suppression of Myc Activity Induces Diapause-like Molecular Profile and Reduces the Effect of Cytotoxic Treatment in Cancer Cells**

(A) 2D GO enrichment comparisons between transcriptional changes induced in MDAMB-231 cells by CRISPR-based *MYC* KO (versus *OR10G2* KO, as control) and those in mouse embryonic diapause (versus normal epiblast; left) and those in docetaxel-persistent MDAMB-231 organoids (versus treatment naive; right).

(B and C) Viability of MDAMB-231 cells with knocked-out *MYC* or *OR10G2* (as control) exposed to 1  $\mu$ M docetaxel for 24 h, visualized microscopically (B; scale bar, 200  $\mu$ m) or measured as percentage of live cells (C; trypan blue assay) (quadruplicates; mean  $\pm$  SEM).

(D) The effect of docetaxel on the viability of MDAMB-231 and MCF7 BrCa cells with KO of *MYC* or control genes *OR10G2* and *OR10G3* in 2D cultures (24 h time point) (quadruplicates; mean  $\pm$  SEM).

(E and F) Abrogation of chemotherapy-induced cytotoxicity in MDAMB-231 (E; 7 days) and MCF7 and ZR75-1 (F; 5 days) organoid cultures by co-treatment with JQ1 (quadruplicates; mean  $\pm$  SEM).

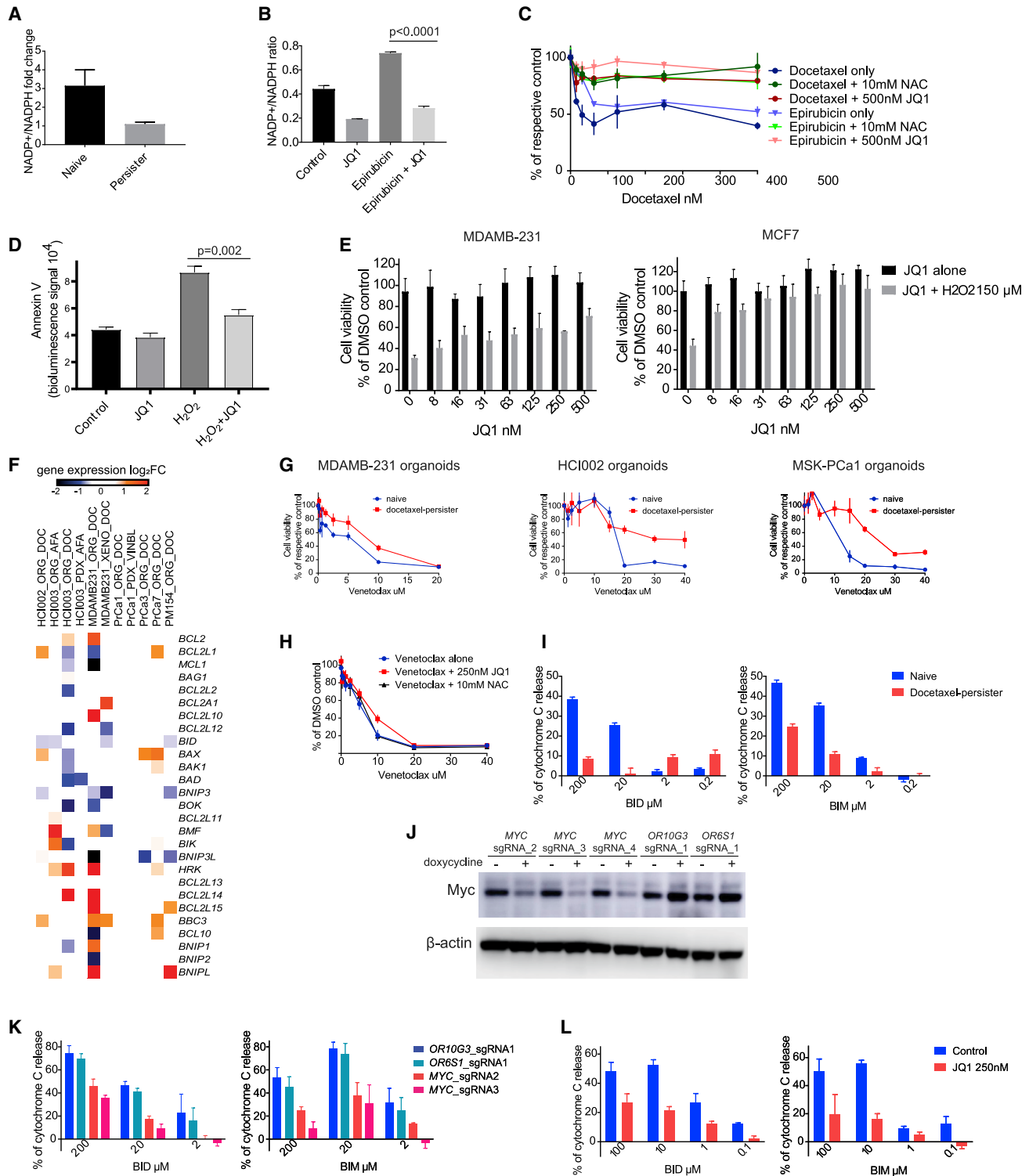


**Figure 5. Suppression of Myc Activity in Cancer Cells Reduces Redox Stress and Attenuates Apoptotic Priming**

(A) Epirubicin-induced redox stress (see STAR Methods) in treatment-naive and docetaxel-persister MDAMB-231 organoids; 24 h (triplicates; mean  $\pm$  SEM). (B) JQ1 (500 nM) effect on redox stress levels in MDAMB-231 cells in the presence of cytotoxic chemotherapy (epirubicin 1  $\mu$ M; 12 h, triplicates; mean  $\pm$  SEM). (C) MDAMB-231 3D organoids treated with docetaxel or epirubicin in the presence versus absence of N-acetylcysteine (NAC) or JQ1 (6 day time point; quadruplicates; mean  $\pm$  SEM). (D and E) Apoptosis (D, 12 h) and viability (E, 24 h) of MDAMB-231 cells treated with H<sub>2</sub>O<sub>2</sub> (150  $\mu$ M) in the presence or absence of JQ1 (500 nM) (quadruplicates; mean  $\pm$  SEM).

(legend continued on next page)

biosynthetic activity and EDL molecular profile (Figure 6G). The transcriptional changes associated with abemaciclib-induced cell-cycle arrest were only weakly correlated with embryonic diapause (Figure 6H, left) and mostly reflected suppression of the mitotic mechanism. In contrast, cell-cycle-arrested cells that subsequently persisted through chemotherapy were distinct from their respective abemaciclib-arrested but chemotherapy-naïve cells, and had an EDL transcriptional adaptation (Figure 6H, right). These results indicate that the diapause-like transcriptional adaptation in chemo-persistent cells can emerge whether exposure to cytotoxic chemotherapy is preceded or not by cell-cycle arrest. Notably, biosynthetic suppression and upregulation of diapause-specific molecular hallmarks were more pronounced in the chemo-persistent cell population versus cycle-arrested cells (Figure 6I). Together, these data suggest that, although both cell-cycle-arrested and chemo-persistent cells display proliferative quiescence, they differ substantially in the magnitude of biosynthetic quiescence and the molecular features of the EDL transcriptional adaptation. Therefore, proliferative quiescence *per se* cannot fully account for the emergence of the chemo-persistent phenotype and its molecular characteristics.

We also examined whether the EDL transcriptional adaptation signature in treatment-persistent cancer cells in our pre-clinical models overlaps with experimentally defined and curated MSigDB signatures of senescence and stemness, cellular states generally associated with treatment resistance. The large majority of core stemness gene sets were not upregulated in treatment-persister cells, and the few stemness signatures that showed similarities with the EDL transcriptional adaptation comprised modules driven by Myc suppression and overlapped with embryonic diapause (which is evidently a physiological adaptation that does not alter stemness *per se*) (Figure S7I). Similar to embryonic diapause (Boroviak et al., 2015), expression of pluripotency genes was retained, but not enriched, in EDL cancer cells at levels comparable to those of pre-treatment organoids, including genes in common with the E4.5 epiblast stage, such as *KLF2*, *KLF4*, *LIFR*, *TBX3*, *IL6ST*, and *JAK3* (in BrCa models) and *SOX2* (in PrCa models) (Figure S8A). In addition, a partial senescence signature was also recurrent in some, but not all, EDL models (Figure S7I), possibly reflecting the suppression of Myc transcriptional output. Furthermore, genetic ablation of p53 in *TP53* wild-type MCF7 cells did not affect the ability of MCF7 organoids to generate TP-organoids with EDL molecular signature after treatment with chemotherapy (data not shown). Interestingly, the oxidative phosphorylation signature (recently reported to be upregulated in some BrCa xenograft chemo-persistence models (Echeverria et al., 2019)) was increased only in non-EDL residual clinical tumors, but was suppressed in the EDL chemo-persister tumors with inactivated Myc (data

not shown), putatively reflecting two distinct treatment-persistent mechanisms in cancer cells.

The transcriptional and proteomic changes associated with biosynthetic activity in TP-organoids were partially reversed to pre-treatment levels within 3 days after drug washout (Figures S8B–S8D). Extensive transcriptional changes for histones (Figures S8C and S8E) and epigenetic modifiers (e.g., *DNMT1*, *DNMT3B*, *NCOA3*, and *TET2*; data not shown) in TP-organoids were also similar to the embryonic diapause (Boroviak et al., 2015) and indicate the implication of epigenetic reprogramming in the acquisition of the EDL state, a theme also proposed in other models of drug tolerance (Sharma et al., 2010; Vinogradova et al., 2016). Interestingly, the demethylase KDM5A, which has been implicated in 2D models of tyrosine kinase inhibitor (TKI) persistence (DTPs, Sharma et al., 2010), was not upregulated in our TP-organoid models or in residual tumors in patients; concordantly, the chemo-persister EDL organoids were not preferentially sensitive to inhibitors of KDM5a, IGF1R, or HDAC (data not shown), which were reported to eliminate DTPs (Sharma et al., 2010; Vinogradova et al., 2016).

Similar to embryonic diapause, which can be induced by various sources of stress (Fenelon et al., 2014; Renfree and Fenelon, 2017), treatment with distinct compound classes resulted in EDL TP-organoids that maintained the core EDL signature reflecting fundamental survival mechanisms (e.g., suppression of biosynthetic activity) but differed in transcriptional changes related to the respective drug's mechanisms of action. For instance, anti-microtubule-persister organoids (but not afatinib persisters) had marked upregulation of genes of the tubulin family, whereas afatinib-persistent organoids (but not docetaxel persisters) had upregulation of the *GSTA* gene family (Figure S8E). Interestingly, afatinib-persistent organoid fractions were sensitive to anti-microtubule agents, whereas anti-microtubule persisters were cross-resistant to afatinib (Figure S8F), suggesting that the EDL state may involve both common and drug-specific molecular features.

### Therapeutic Implications of Treatment-Persister Diapause-like Tumor Cells

Treatment-persistent residual tumor cells represent an important barrier to curative outcomes. Therefore, a better understanding of the therapeutic vulnerabilities of the EDL state potentially has major clinical implications. We examined two distinct approaches to therapeutically targeting treatment-persistent residual tumor cells, by preventing them from exiting the EDL state after the stop of cytotoxic treatment and by exposing them to therapeutics that may be highly active against EDL cells.

Given the transient and reversible nature of the EDL state, we reasoned that, after the end of the cytotoxic treatment, it might be therapeutically possible to prevent tumor cells from exiting

(F) Transcriptional changes (compared with vehicle) in apoptosis-related BCL2 family genes in treatment-persister organoids and PDX models.

(G) Sensitivity of naïve and docetaxel-persister organoid models to venetoclax (72 h) (quadruplicates, mean ± SEM).

(H) Sensitivity of MDAMB-231 cells to venetoclax in presence or absence of JQ1 or N-acetylcysteine (72 h) (quadruplicates, mean ± SEM).

(I) Comparing apoptotic priming between docetaxel-persister TP-organoids and their naïve counterparts using the BH3 profiling method (Montero et al., 2015) (triplicates; mean ± SEM).

(J) Western blot showing downregulation of Myc protein in MDAMB-231 cells via doxycycline-inducible CRISPRi.

(K and L) Comparing apoptotic priming, using BH3 profiling, in MDAMB-231 cells with CRISPRi against *MYC* or (as controls) *OR10G3* or *OR6S1* (K) or JQ1 (L) (triplicates; mean ± SEM).

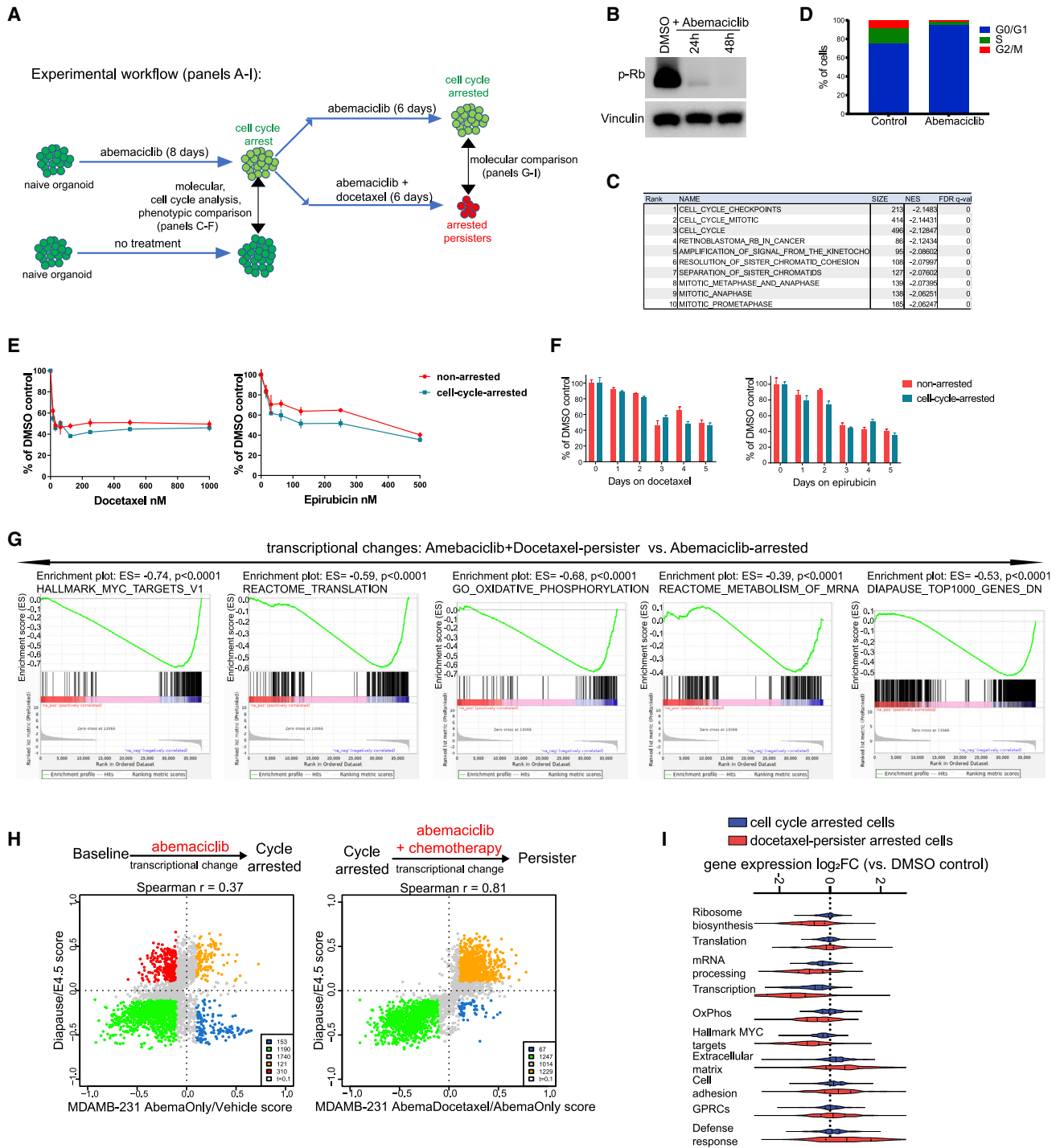


**Figure 6. The Diapause-like Treatment-Persister Adaptation Involves Distinct Features beyond Proliferative Quiescence**

(A) Schematic representation of the experiment.  
 (B) Dephosphorylation of Rb in MDAMB-231 organoids after treatment with 500 nM abemaciclib.  
 (C and D) Suppression of transcriptional signatures for cell-cycle molecular mechanisms (C, top 10 terms for negative enrichment in cell-cycle-arrested organoids) and of cell-cycle progression (D, cell-cycle analysis) in MDAMB-231 organoids after treatment with abemaciclib (8 days).  
 (E and F) Dose (5 days time-point, E) and time-lapse (1  $\mu$ M concentration, F) response of non-arrested and abemaciclib-arrested MDAMB-231 organoids to cytotoxic agents (quadruplicates; mean  $\pm$  SEM).  
 (G) Gene set enrichment plots depicting transcriptional changes in chemo-persister cell-cycle-arrested organoid fractions (obtained by longitudinal treatment of abemaciclib-arrested organoids with docetaxel to generate persister cell population) versus their respective cell-cycle-arrested baseline (obtained by treatment with abemaciclib only).

dormancy by exposing them to therapeutics that can sustain that state. Inhibition of Myc and mTOR has been shown to maintain mouse embryos cultured *ex vivo* in diapause (Bulut-Karslioglu et al., 2016; Scognamiglio et al., 2016). Concordantly, we observed that treating EDL persister organoids with JQ1 or the mTOR inhibitor INK028 retained these cells in a dormant state and prevented their regrowth (Figure 7A).

Importantly, most upregulated transcripts in TP-organoids and chemo-persister PDX fractions were not linked to genes essential for *in vitro* survival or proliferation of cancer cell lines in 2D cultures (Figure S9A), indicating the distinct value of TP-organoid models to inform on survival mechanisms emerging in residual treatment-persister tumors. We therefore reasoned that the EDL state might exhibit distinct therapeutic vulnerabilities. To assess the therapeutic landscape of the EDL cancer cell state and identify specific vulnerabilities of chemo-persister cells, we tested the sensitivity of TP-organoids to a diverse library of ~500 compounds, which included FDA-approved chemotherapeutics and targeted agents, compounds targeting transcriptional and epigenetic mechanisms putatively involved in the diapause-like transcriptional program, and other drug classes. The chemo-persistent EDL cancer cells were refractory or resistant to most classes of broad-spectrum cytotoxic agents (e.g., anthracyclins, taxanes, vinca alkaloids, proteasome inhibitors) and tended to have reduced sensitivity to other compound classes, including HDAC inhibitors (Figures 7B–7D).

Inhibition of autophagy, a mechanism involved in drug resistance in cancer, reduced the ability of mouse embryonic stem cells to survive *ex vivo* in a diapause-like state (Bulut-Karslioglu et al., 2016). Pharmacological targeting of autophagy in our organoids enhanced the acute cytotoxicity of docetaxel against treatment-naïve cells but had negligible efficacy against TP-organoids (Figure S9B), indicating that autophagy may contribute to tumor cell entry into the EDL state, but once the cells acquire that state, autophagy may not be essential for sustained survival of the chemotherapy-persistent cells. Similarly, targeting the DNA damage mechanisms (e.g., ATR) synergized with cytotoxic therapy in treatment-naïve organoids, but was ineffective in EDL TP-organoids (Figure S9C).

Notably, phenotypic screens revealed unanticipated increases in sensitivity of TP-organoids to inhibitors of the transcriptional regulator CDK9 (Figure 7E). CDK9 inhibition in TP-organoids derepressed their metabolic and biosynthetic transcriptional signatures and partially reversed their Myc-suppressed diapause-like cell state (Figures 7F–7H), which may explain at least partly the restoration of their sensitivity to chemotherapeutics. Concordant with these *in vitro* observations, co-administration of chemotherapy and CDK9 inhibitor dramatically increased the anti-tumor effect of the former in xenograft studies (Figure 7I and 7J). These observations indicate that targeting the transcriptional adaptation mechanisms that operate during the emergence of the EDL state in residual disease could become a viable therapeutic approach against this cancer cell state.

## DISCUSSION

Conventional chemotherapy and other cytotoxic agents are a cornerstone in cancer treatment, but the molecular properties and therapeutic vulnerabilities of residual tumor cells persisting through cytotoxic therapies remain elusive. The paucity of studies focusing on the comprehensive molecular characterization of residual tumors in patients, or even in animal models, where access to tumor samples during treatment is less limited, reflects a relative underappreciation of this cancer cell state as a distinct barrier to therapeutic efficacy. On the other hand, the mechanistic dissection of the chemo-persistent state has been challenging because the faithful *in vitro* modeling of this cancer cell state is very limited in 2D cultures, where cells are typically eradicated by continuous exposure to cytotoxic chemotherapeutics. Three-dimensional tumor cell cultures (Drost and Clevers, 2018; Weaver et al., 2002) may capture distinct aspects of cancer biology by mimicking the tumor architecture and are used empirically to test drug candidates in short-term assays, but their relevance as a system to study the biology of the drug-persistent cancer cell state had not been examined. We simulated the emergence of drug-persistent residual tumors using 3D organoids and xenograft models amenable to studying this cancer cell state. The drug-persistent cells in 3D models do not appear to emanate stochastically from rare cancer cells within the population (as in previous 2D models of drug persistence; Hata et al., 2016; Sharma et al., 2010), but consisted of substantial TP-organoid fractions surviving the acute cytotoxic effect within most organoids (Figures 1B, 1D, S1E and S2C).

A transient “stress-endurance mode” is a widely accepted concept in developmental biology, where normal epiblasts survive under adverse conditions by transitioning to the distinct, dormant, stage of diapaused epiblast (Boroviak et al., 2015; Fenelon et al., 2014; Renfree and Fenelon, 2017). We show that tumor cells in cancer organoids and PDX models and a substantial proportion of patient tumors can also persist throughout the exposure to cytotoxic drugs, through a molecular adaptation resembling that of embryonic diapause. Similar to diapause, drug-persistent tumor cells are biosynthetically and proliferatively quiescent. However, cell-cycle arrest *per se* did not fully account for chemotherapy persistence (Figure 6). Although similarities between tumors and undifferentiated embryos have been long recognized, our results point to a previously underappreciated link between cancer and normal development, namely, that in both biological settings (cancer and development) the stress-persistent cells (drug-persister cancer cells and diapaused epiblast) are molecularly and phenotypically distinct from their unperturbed counterparts (untreated cancer cells and normal pluripotent epiblast, respectively). Our mechanistic studies indicate that the suppression of Myc is a common mechanism between these two biological settings, suggesting an evolutionarily conserved transcriptional and metabolic program that promotes survival of eukaryotic cells under stress.

(H) 2D GO analysis showing correlation of transcriptional changes induced in cell-cycle-arrested (abemaciclib-arrested versus untreated; left), or in cell-cycle-arrested treatment-persister (abemaciclib-arrested and chemo-persister versus abemaciclib-arrested; right), MDAMB-231 organoids with transcriptional changes in embryonic diapause.

(I) Expression of hallmark transcriptional modules of embryonic diapause in cell-cycle-arrested and in arrested treatment-persister MDAMB-231 organoids (versus naïve).

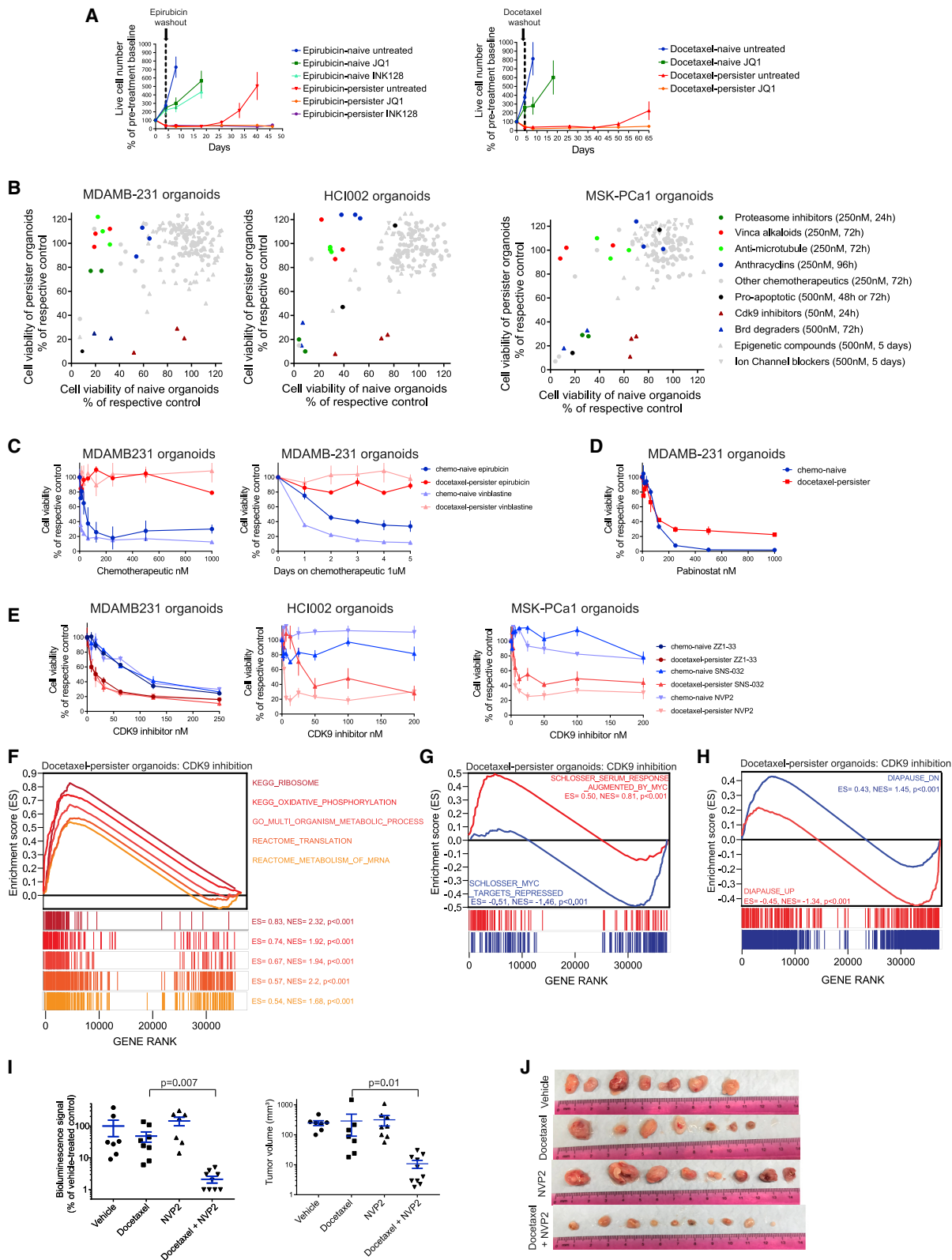


**Figure 7. Diapause-like Persister Organoids Have Distinct Therapeutic Vulnerabilities**

(A) Effect of JQ1 and INK128 on the regrowth of EDL epirubicin-persister or docetaxel-persister MDAMB-231 organoids after chemotherapeutic washout (triplicates; mean  $\pm$  SEM).

(legend continued on next page)

Collectively, our observations demonstrate that tumors can co-opt an embryonic survival mechanism related to reproductive fitness that is widespread across the animal kingdom (Fenelon et al., 2014; Renfree and Fenelon, 2017) and resonate with a view of cancer as an aberrant and regressive developmental process (Soto and Sonnenschein, 2005; Visvader, 2009). Further studies will be needed to dissect the mechanistic links between cellular stress sensing and diapause-like adaptation in different tumor types and molecular contexts, the contribution of the distinct diapause features (e.g., cell-ECM interactions and cell inflammatory response) to the adaptive treatment persistence, and the molecular and functional similarities or differences between the treatment-induced diapause-like adaptation and cancer dormancy in specialized niches (Aguirre-Ghiso, 2007; Phan and Croucher, 2020).

Our study complements and extends prior knowledge on Myc biology. Exogenously controllable Myc deactivation, applied as a primary perturbation against genetically engineered mouse tumors, induces residual dormant tumor cells, which restore the neoplastic features once Myc is reactivated (Lin et al., 2013; Shachaf et al., 2004). Distinct from these prior observations, our current study documents that cancer cells challenged with cytotoxic treatments have the potential to respond by dynamically inactivating Myc, enabling entry into a biosynthetically paused adaptive drug-persistent state, which prevents the complete tumor eradication. This adaptive response for survival through drug-induced stress mimics embryonic diapause. In the absence of cytotoxic treatment, increased Myc activity provides a growth advantage for cancer cells. However, abnormal activation of Myc can also increase baseline redox stress, DNA damage levels, and propensity for apoptosis (Barlow et al., 2013; Evan et al., 1992; McMahon, 2014; Meyer et al., 2006; Vafa et al., 2002). These observations are aligned with our findings that the chemotherapeutic cytotoxic effect can be attenuated in cancer cells that assume low Myc activity during drug exposure.

This diapause-like low-Myc adaptation is reversible. Our drug-washout experiments indicate that chemo-persistent residual tumor cells maintain their malignant potential despite the Myc suppression, reminiscent of tumor regrowth after controllable Myc reactivation in transgenic mouse models. Reactivation of Myc is likely necessary for EDL tumor cells to exit dormancy and resume tumor growth, but fine-tuned gain-of-function studies are needed to determine whether it is sufficient. Our longitudinal experiment with JQ1 treatment after chemotherapeutic washout suggests that continuous Myc suppression can maintain cancer organoids in the dormant state and prevent their regrowth (Figure 7A). Although BET bromodomain and mTOR inhibition have been pursued therapeutically (Alzahrani, 2019; Cochran et al., 2019), these efforts have typically focused on using these thera-

peutic classes, alone or in combination with others, to decrease the burden of established tumors, rather than to prevent the regrowth of dormant residual ones. Our results point to the need for careful pre-clinical assessment of the combination of Myc-suppressing agents with cytotoxic chemotherapy, to avoid antagonistic interactions between them. Interestingly, our results also indicate that BET bromodomain or mTOR inhibition merits further investigation as part of maintenance therapy after the completion of cytotoxic treatment.

Targeting the diapause-like transcriptional adaptation in drug-persistent cells might be a therapeutic approach to eliminate residual tumors. Our phenotypic screens revealed that chemo-persistent cancer cells are preferentially sensitive to inhibitors of CDK9. This observation is concordant with studies showing that CDK9 inhibition is associated with rebound activation of Myc in some cellular contexts (Lu et al., 2015). These data suggest that this drug class (currently in clinical development) merits further examination of its potential to target chemo-persistent tumor cells. Overall, our results enhance the rationale for the investigation of novel therapeutic approaches to specifically target the residual EDL cancer cells and therefore prevent tumor evolution to new forms of acquired resistance.

The hypothesis that residual disease after cytotoxic treatment is a problem of reversible drug persistence resonates with clinical observations that recurrent tumors may occasionally respond to the same chemotherapeutic after a “drug holiday” (Cara and Tannock, 2001). These observations, together with our findings presented here, indicate that genetic resistance may not be the only or primary mechanism responsible for residual tumors following treatment. The EDL treatment-persistent tumors are a crucial link in the evolution of chemoresistance, as they provide the reservoir of cancer cells from which other, genetic or epigenetic, mechanisms of acquired resistance can subsequently emerge (a similar hypothesis has been proposed for TKI tolerance models in 2D cultures; Hata et al., 2016). Dissecting the detailed mechanisms by which tumor cells enter, survive through, and exit this dormant diapause-like stage can lead to new therapeutic approaches against one or more of these cancer cell states in patients and increase the likelihood for cures. Distinct from other 2D and 3D culture models of cancer, the diapause-like TP-organoids constitute a clinically relevant platform to evaluate drug candidates that specifically target the treatment-persistent residual tumors that is amenable to drug-discovery efforts.

## STAR★METHODS

Detailed methods are provided in the online version of this paper and include the following:

(B–D) Sensitivity of docetaxel-naive and docetaxel-persister organoid models MDAMB-231, HCl002, and MSK-PCa1 to 176 compounds of various classes (B) and examples of validation by time-lapse and/or fixed time-point assays for selected chemotherapeutics (C, 72 h) and epigenetic (D, 96 h) agents (quadruplicates; mean  $\pm$  SEM).

(E) Sensitivity of naive and docetaxel-persister organoids to a heterobifunctional degrader of CDK9 (ZZ1-33; see STAR Methods) and CDK9 inhibitors (NVP2 and SNS032) (48 h) (Olson et al., 2018) (quadruplicates; mean  $\pm$  SEM).

(F–H) Transcriptional changes induced in MDAMB-231 TP-organoids after 24 h exposure to CDK9 inhibitor NVP2, depicted as gene set enrichment plots for biosynthetic and metabolic activity (F), Myc activity (G), and mouse embryonic diapause signature (H).

(I and J) *In vivo* effect of chemotherapy, CDK9 inhibitor NVP2, and combination treatment on MDAMB-231 xenograft growth. Tumor responses after 4 weeks treatment (I; mean values and SEM shown in blue) and images of harvested tumors at the end of the experiment (J).

- **KEY RESOURCES TABLE**
- **RESOURCE AVAILABILITY**
  - Lead Contact
  - Materials Availability
  - Data and Code Availability
- **EXPERIMENTAL MODEL AND SUBJECT DETAILS**
  - Cell Lines
  - Patient-Derived Models
- **METHOD DETAILS**
  - Reagents
  - 3D Cultures
  - Whole Exome Sequence Analysis of Patient-Derived Cancer Models
  - Persister vs Vehicle Exome Sequencing Analysis
  - Cell Viability Assays
  - EDL Organoids Regrowth Suppression Experiment
  - PRISM-based Phenotypic Studies in Pools of Bar-coded Cancer Cell Lines
  - Barcode-Mediated Clonal Tracking Experiment
  - Analysis of Clonal Composition Using Sequenced Barcodes
  - NADPH/NADP Measurement Assay
  - Apoptosis Assay
  - BH3 Profiling
  - Cell Cycle Analyses
  - Histological Analyses
  - Western Blot
  - CRISPR-Cas9 Mediated MYC Gene Knockout
  - CRISPR-interference Mediated MYC Gene Knockdown
  - Myc Overexpression
  - Animal Studies
  - Proteomic Analysis (Reverse Phase Protein Analysis, RPPA)
  - Sample Collection and Gene Expression Analysis
  - Public Datasets Used
  - Human to Mouse Orthologous Gene Mapping
  - Gene Set Enrichment Analysis (GSEA)
  - Embryonic Diapause-like (EDL) Signature Score, EDL Proneness Signature and Survival Analysis
  - Pairwise 2D GO Analysis
  - Gene Essentiality Data
- **QUANTIFICATION AND STATISTICAL ANALYSIS**

#### SUPPLEMENTAL INFORMATION

Supplemental Information can be found online at <https://doi.org/10.1016/j.ccell.2020.12.002>.

#### ACKNOWLEDGMENTS

We thank Nicholas Navin, Ruli Gao (UT MD Anderson Cancer Center), Theodoros Foukakis (Karolinska Institutet), and Ingrid Hedenfalk (Lund University Cancer Center) for providing information about the patient molecular data. We thank Keith Blackwell (Joslin Diabetes Center), Andrew Kung (MSKCC), Todd Golub (Broad Institute), William Hahn (DFCI/Broad Institute), Ana Soto and Carlos Sonnenschein (Tufts University), Toshihiro Shioda (MGH), Bruce Zetter (Boston Children's Hospital), and William Kaelin (DFCI) for useful discussions and advice. We also thank Megan Bariteau and Jeffrey Sorrell for administrative and organizational support of the study. Funding for this work was from the Breast Cancer Alliance Young Investigator Award (E.D., C.S.M.),

the Claudia Adams Barr Program for Innovative Cancer Research (E.D., M.S., C.S.M.), the Hellenic Women's Club (C.S.M., E.D.), a Terri Brodeur Breast Cancer Foundation grant (E.D.), the Avon Foundation Breast Cancer Research Program (C.S.M., E.D.), an Elsa U. Pardee Foundation grant (C.S.M., E.D.), Department of Defense grant W81XWH-15-1-0012 (A.C.C., C.S.M.), the Ludwig Center at Harvard (C.S.M.), the Leukemia and Lymphoma Society Scholar Award (C.S.M.), and NIH R01 grant CA179483 (C.S.M., N.S.G.). Processing of raw CRISPR and RNA-sequencing data was performed on the Orchestra High-Performance Compute Cluster at Harvard Medical School (grant NCCR 1S10RR028832-01, <http://rc.hms.harvard.edu>).

#### AUTHOR CONTRIBUTIONS

E.D. and C.S.M. conceived the project. E.D. designed and executed or supervised the execution of the experiments and analyzed the data. R.d.M.S., A.C.C., and B.B. performed bioinformatic analyses and visualization. D.K., S.S., X.W., P.A., J.B., J.R., H.T., Z.L., L.W., S.B., B.G., J.B., Z.L., M.S., and R.S. performed experiments or assisted in their execution. A.A.K., N.S.G., F.V., R.J., A.T., I.G., J.R., Y.C., D.G., A.W., C.D., A.M., and M.B. provided models or input with data analysis and interpretation. E.D. and C.S.M. wrote the manuscript with input from the co-authors.

#### DECLARATION OF INTERESTS

E.D. and C.S.M. are co-inventors on a patent related to the use of 3D cultures. Y.C. reports personal fees from Oric Pharmaceuticals outside the submitted work. R.J. reports research funding from Pfizer and Lilly and consulting for Carriack and Luminex. M.B. reports sponsored research support from Novartis; serves on the science advisory board (SAB) of and received fees from Kronos Bio, GV20 Oncotherapy, and H3 Biomedicine; and holds equity in Kronos Bio and GV20 Oncotherapy. N.S.G. is a founder, SAB member, and equity holder in Gatekeeper, Syros, Petra, C4, Allorion, Jengu, Inception, B2S, and Soltego (board member) and his lab receives or has received research funding from Novartis, Takeda, Astellas, Taiho, Jansen, Kinogen, Her2Lc, Deerfield, and Sanofi. C.S.M. discloses research funding from Janssen/Johnson & Johnson, Teva, EMD Serono, Abbvie, Arch Oncology, Karyopharm, Sanofi, and Nurix; employment of a relative with Takeda; and consultant/honoraria from Fate Therapeutics, Ionis Pharmaceuticals, and FIMECS.

Received: January 31, 2020

Revised: October 19, 2020

Accepted: December 2, 2020

Published: January 7, 2021

#### REFERENCES

- Aguirre-Ghiso, J.A. (2007). Models, mechanisms and clinical evidence for cancer dormancy. *Nat. Rev. Cancer* 7, 834–846.
- Al'Khafaji, A., Gutierrez, C., Brenner, E., Durrett, R., Johnson, K.E., Zhang, W., Li, S., Livak, K.J., Neuberg, D., Brock, A., and Wu, C.J. (2019). Expressed barcodes enable clonal characterization of chemotherapeutic responses in chronic lymphocytic leukemia. *bioRxiv*. <https://doi.org/10.1101/761981>.
- Alzahrani, A.S. (2019). PI3K/Akt/mTOR inhibitors in cancer: at the bench and bedside. *Semin. Cancer Biol.* 59, 125–132.
- Ashburner, M., Ball, C.A., Blake, J.A., Botstein, D., Butler, H., Cherry, J.M., Davis, A.P., Dolinski, K., Dwight, S.S., Eppig, J.T., et al. (2000). Gene ontology: tool for the unification of biology. *The Gene Ontology Consortium. Nat. Genet.* 25, 25–29.
- Barlow, J.H., Faryabi, R.B., Callen, E., Wong, N., Malhowski, A., Chen, H.T., Gutierrez-Cruz, G., Sun, H.W., McKinnon, P., Wright, G., et al. (2013). Identification of early replicating fragile sites that contribute to genome instability. *Cell* 152, 620–632.
- Benjamini, Y., and Hochberg, Y. (1995). Controlling the false discovery rate: a practical and powerful approach to multiple testing. *J. R. Stat. Soc. Ser. B (Methodological)* 57, 289–300.

- Blake, J.A., Eppig, J.T., Kadin, J.A., Richardson, J.E., Smith, C.L., and Bult, C.J. (2017). Mouse Genome Database (MGD)-2017: community knowledge resource for the laboratory mouse. *Nucleic Acids Res.* *45*, d723–d729.
- Boroviak, T., Loos, R., Lombard, P., Okahara, J., Behr, R., Sasaki, E., Nichols, J., Smith, A., and Bertone, P. (2015). Lineage-specific profiling delineates the emergence and progression of naive pluripotency in mammalian embryogenesis. *Dev. Cell* *35*, 366–382.
- Breitling, R., Armengaud, P., Amtmann, A., and Herzyk, P. (2004). Rank products: a simple, yet powerful, new method to detect differentially regulated genes in replicated microarray experiments. *FEBS Lett.* *573*, 83–92.
- Bulut-Karslioglu, A., Biechele, S., Jin, H., Macrae, T.A., Hejna, M., Gertsenstein, M., Song, J.S., and Ramalho-Santos, M. (2016). Inhibition of mTOR induces a paused pluripotent state. *Nature* *540*, 119–123.
- Cara, S., and Tannock, I.F. (2001). Retreatment of patients with the same chemotherapy: implications for clinical mechanisms of drug resistance. *Ann. Oncol.* *12*, 23–27.
- Carlson, M.R., Pages, H., Arora, S., Obenchain, V., and Morgan, M. (2016). Genomic annotation resources in R/bioconductor. *Methods Mol. Biol.* *1418*, 67–90.
- Cochran, A.G., Conery, A.R., and Sims, R.J., 3rd (2019). Bromodomains: a new target class for drug development. *Nat. Rev. Drug Discov.* *18*, 609–628.
- Cortazar, P., Zhang, L., Untch, M., Mehta, K., Costantino, J.P., Wolmark, N., Bonnefoi, H., Cameron, D., Gianni, L., Valagussa, P., et al. (2014). Pathological complete response and long-term clinical benefit in breast cancer: the CTNeoBC pooled analysis. *Lancet* *384*, 164–172.
- Cox, J., and Mann, M. (2012). 1D and 2D annotation enrichment: a statistical method integrating quantitative proteomics with complementary high-throughput data. *BMC Bioinformatics* *13* (Suppl 16), S12.
- Delmore, J.E., Issa, G.C., Lemieux, M.E., Rahl, P.B., Shi, J., Jacobs, H.M., Kastriitis, E., Gilpatrick, T., Paranal, R.M., Qi, J., et al. (2011). BET bromodomain inhibition as a therapeutic strategy to target c-Myc. *Cell* *146*, 904–917.
- DeRose, Y.S., Wang, G., Lin, Y.C., Bernard, P.S., Buys, S.S., Ebbert, M.T., Factor, R., Matsen, C., Milash, B.A., Nelson, E., et al. (2011). Tumor grafts derived from women with breast cancer authentically reflect tumor pathology, growth, metastasis and disease outcomes. *Nat. Med.* *17*, 1514–1520.
- Dhimolea, E., de Matos Simoes, R., Kansara, D., Weng, X., Sharma, S., Awate, P., Liu, Z., Gao, D., Mitsiades, N., Schwab, J.H., et al. (2020). Pleiotropic mechanisms drive endocrine resistance in the three-dimensional bone microenvironment. *Cancer ResCAN-20-0571*. <https://doi.org/10.1158/0008-5472.CAN-20-0571>.
- Dhimolea, E., Maffini, M.V., Soto, A.M., and Sonnenschein, C. (2010). The role of collagen reorganization on mammary epithelial morphogenesis in a 3D culture model. *Biomaterials* *31*, 3622–3630.
- Drost, J., and Clevers, H. (2018). Organoids in cancer research. *Nat. Rev. Cancer* *18*, 407–418.
- Durinck, S., Spellman, P.T., Birney, E., and Huber, W. (2009). Mapping identifiers for the integration of genomic datasets with the R/Bioconductor package biomaRt. *Nat. Protoc.* *4*, 1184–1191.
- Echeverria, G.V., Ge, Z., Seth, S., Zhang, X., Jeter-Jones, S., Zhou, X., Cai, S., Tu, Y., McCoy, A., Peoples, M., et al. (2019). Resistance to neoadjuvant chemotherapy in triple-negative breast cancer mediated by a reversible drug-tolerant state. *Sci. Transl. Med.* *11*, eaav0936.
- Evan, G.I., Wyllie, A.H., Gilbert, C.S., Littlewood, T.D., Land, H., Brooks, M., Waters, C.M., Penn, L.Z., and Hancock, D.C. (1992). Induction of apoptosis in fibroblasts by c-myc protein. *Cell* *69*, 119–128.
- Fenelon, J.C., Banerjee, A., and Murphy, B.D. (2014). Embryonic diapause: development on hold. *Int. J. Dev. Biol.* *58*, 163–174.
- Gao, D., Vela, I., Sboner, A., Iaquinata, P.J., Karthaus, W.R., Gopalan, A., Dowling, C., Wanjala, J.N., Undvall, E.A., Arora, V.K., et al. (2014). Organoid cultures derived from patients with advanced prostate cancer. *Cell* *159*, 176–187.
- Gonzalez-Angulo, A.M., Iwamoto, T., Liu, S., Chen, H., Do, K.A., Hortobagyi, G.N., Mills, G.B., Meric-Bernstam, F., Symmans, W.F., and Pusztai, L. (2012). Gene expression, molecular class changes, and pathway analysis after neoadjuvant systemic therapy for breast cancer. *Clin. Cancer Res.* *18*, 1109–1119.
- Gruosso, T., Mieulet, V., Cardon, M., Bourachot, B., Kieffer, Y., Devun, F., Dubois, T., Dutreix, M., Vincent-Salomon, A., Miller, K.M., and Mechtak-Grigoriou, F. (2016). Chronic oxidative stress promotes H2AX protein degradation and enhances chemosensitivity in breast cancer patients. *EMBO Mol. Med.* *8*, 527–549.
- Hata, A.N., Niederst, M.J., Archibald, H.L., Gomez-Caraballo, M., Siddiqui, F.M., Mulvey, H.E., Maruvka, Y.E., Ji, F., Bhang, H.E., Krishnamurthy Radhakrishna, V., et al. (2016). Tumor cells can follow distinct evolutionary paths to become resistant to epidermal growth factor receptor inhibition. *Nat. Med.* *22*, 262–269.
- Kamburov, A., Stelzl, U., Lehrach, H., and Herwig, R. (2013). The ConsensusPathDB interaction database: 2013 update. *Nucleic Acids Res.* *41*, D793–D800.
- Keams, N.A., Genga, R.M., Enuameh, M.S., Garber, M., Wolfe, S.A., and Maehr, R. (2014). Cas9 effector-mediated regulation of transcription and differentiation in human pluripotent stem cells. *Development (Cambridge, England)* *141*, 219–223.
- Kim, C., Gao, R., Sei, E., Brandt, R., Hartman, J., Hatschek, T., Crosetto, N., Foukakis, T., and Navin, N.E. (2018). Chemoresistance evolution in triple-negative breast cancer delineated by single-cell sequencing. *Cell* *173*, 879–893.e813.
- Kimbung, S., Markholm, I., Bjohle, J., Lekberg, T., von Wachenfeldt, A., Azavedo, E., Saracco, A., Hellstrom, M., Veerla, S., Paquet, E., et al. (2018). Assessment of early response biomarkers in relation to long-term survival in patients with HER2-negative breast cancer receiving neoadjuvant chemotherapy plus bevacizumab: results from the Phase II PROMIX trial. *Int. J. Cancer* *142*, 618–628.
- Kolesnikov, N., Hastings, E., Keays, M., Melnichuk, O., Tang, Y.A., Williams, E., Dylag, M., Kurbatova, N., Brandizi, M., Burdett, T., et al. (2015). ArrayExpress update—simplifying data submissions. *Nucleic Acids Res.* *43*, D1113–D1116.
- Li, H., and Durbin, R. (2009). Fast and accurate short read alignment with Burrows-Wheeler transform. *Bioinformatics* *25*, 1754–1760.
- Li, W., Xu, H., Xiao, T., Cong, L., Love, M.I., Zhang, F., Irizarry, R.A., Liu, J.S., Brown, M., and Liu, X.S. (2014). MAGeCK enables robust identification of essential genes from genome-scale CRISPR/Cas9 knockout screens. *Genome Biol.* *15*, 554.
- Liao, Y., Smyth, G.K., and Shi, W. (2014). featureCounts: an efficient general purpose program for assigning sequence reads to genomic features. *Bioinformatics* *30*, 923–930.
- Lin, W.C., Rajbhandari, N., Liu, C., Sakamoto, K., Zhang, Q., Triplett, A.A., Batra, S.K., Opavsky, R., Felsher, D.W., DiMaio, D.J., et al. (2013). Dormant cancer cells contribute to residual disease in a model of reversible pancreatic cancer. *Cancer Res.* *73*, 1821–1830.
- Love, M.I., Huber, W., and Anders, S. (2014). Moderated estimation of fold change and dispersion for RNA-seq data with DESeq2. *Genome Biol.* *15*, 550.
- Loven, J., Hoke, H.A., Lin, C.Y., Lau, A., Orlando, D.A., Vakoc, C.R., Bradner, J.E., Lee, T.I., and Young, R.A. (2013). Selective inhibition of tumor oncogenes by disruption of super-enhancers. *Cell* *153*, 320–334.
- Lu, H., Xue, Y., Yu, G.K., Arias, C., Lin, J., Fong, S., Faure, M., Weisburd, B., Ji, X., Mercier, A., et al. (2015). Compensatory induction of MYC expression by sustained CDK9 inhibition via a BRD4-dependent mechanism. *Elife* *4*, e06535.
- Luo, J., Solimini, N.L., and Elledge, S.J. (2009). Principles of cancer therapy: oncogene and non-oncogene addiction. *Cell* *136*, 823–837.
- Magbanua, M.J., Wolf, D.M., Yau, C., Davis, S.E., Crothers, J., Au, A., Haqq, C.M., Livasy, C., Rugo, H.S., Esserman, L., et al. (2015). Serial expression analysis of breast tumors during neoadjuvant chemotherapy reveals changes in cell cycle and immune pathways associated with recurrence and response. *Breast Cancer Res.* *17*, 73.
- McKenna, A., Hanna, M., Banks, E., Sivachenko, A., Cibulskis, K., Kernytsky, A., Garimella, K., Altshuler, D., Gabriel, S., Daly, M., and DePristo, M.A. (2010).

The Genome Analysis Toolkit: a MapReduce framework for analyzing next-generation DNA sequencing data. *Genome Res.* 20, 1297–1303.

McMahon, S.B. (2014). MYC and the control of apoptosis. *Cold Spring Harbor Perspect. Med.* 4, a014407.

McMillin, D.W., Delmore, J., Negri, J.M., Vanneman, M., Koyama, S., Schlossman, R.L., Munshi, N.C., Laubach, J., Richardson, P.G., Dranoff, G., et al. (2012). Compartment-Specific Bioluminescence Imaging platform for the high-throughput evaluation of antitumor immune function. *Blood* 119, e131–138.

Meyer, N., Kim, S.S., and Penn, L.Z. (2006). The Oscar-worthy role of Myc in apoptosis. *Semin. Cancer Biol.* 16, 275–287.

Meyers, R.M., Bryan, J.G., McFarland, J.M., Weir, B.A., Sizemore, A.E., Xu, H., Dharia, N.V., Montgomery, P.G., Cowley, G.S., Pantel, S., et al. (2017). Computational correction of copy number effect improves specificity of CRISPR-Cas9 essentiality screens in cancer cells. *Nat. Genet.* 49, 1779–1784.

Montero, J., Sarosiek, K.A., DeAngelo, J.D., Maertens, O., Ryan, J., Ercan, D., Piao, H., Horowitz, N.S., Berkowitz, R.S., Matulonis, U., et al. (2015). Drug-induced death signaling strategy rapidly predicts cancer response to chemotherapy. *Cell* 160, 977–989.

Olson, C.M., Jiang, B., Erb, M.A., Liang, Y., Doctor, Z.M., Zhang, Z., Zhang, T., Kwiatkowski, N., Boukhali, M., Green, J.L., et al. (2018). Pharmacological perturbation of CDK9 using selective CDK9 inhibition or degradation. *Nat. Chem. Biol.* 14, 163–170.

Phan, T.G., and Croucher, P.I. (2020). The dormant cancer cell life cycle. *Nat. Rev. Cancer* 20, 398–411.

Ramos, A.H., Lichtenstein, L., Gupta, M., Lawrence, M.S., Pugh, T.J., Saksena, G., Meyerson, M., and Getz, G. (2015). Oncotator: cancer variant annotation tool. *Hum. Mutat.* 36, E2423–E2429.

Renfree, M.B., and Fenelon, J.C. (2017). The enigma of embryonic diapause. *Development* 144, 3199–3210.

Ryan, J., Montero, J., Rocco, J., and Letai, A. (2016). iBH3: simple, fixable BH3 profiling to determine apoptotic priming in primary tissue by flow cytometry. *Biol. Chem.* 397, 671–678.

Schumacker, P.T. (2006). Reactive oxygen species in cancer cells: live by the sword, die by the sword. *Cancer Cell* 10, 175–176.

Scognamiglio, R., Cabezas-Wallscheid, N., Thier, M.C., Altamura, S., Reyes, A., Prendergast, A.M., Baumgartner, D., Carnevalli, L.S., Atzberger, A.,

Haas, S., et al. (2016). Myc depletion induces a pluripotent dormant state mimicking diapause. *Cell* 164, 668–680.

Shachaf, C.M., Kopelman, A.M., Arvanitis, C., Karlsson, A., Beer, S., Mandl, S., Bachmann, M.H., Borowsky, A.D., Ruebner, B., Cardiff, R.D., et al. (2004). MYC inactivation uncovers pluripotent differentiation and tumour dormancy in hepatocellular cancer. *Nature* 431, 1112–1117.

Sharma, S.V., Lee, D.Y., Li, B., Quinlan, M.P., Takahashi, F., Maheswaran, S., McDermott, U., Azizian, N., Zou, L., Fischbach, M.A., et al. (2010). A chromatin-mediated reversible drug-tolerant state in cancer cell subpopulations. *Cell* 141, 69–80.

Soto, A.M., and Sonnenschein, C. (2005). Emergentism as a default: cancer as a problem of tissue organization. *J. Biosci.* 30, 103–118.

Subramanian, A., Tamayo, P., Mootha, V.K., Mukherjee, S., Ebert, B.L., Gillette, M.A., Paulovich, A., Pomeroy, S.L., Golub, T.R., Lander, E.S., and Mesirov, J.P. (2005). Gene set enrichment analysis: a knowledge-based approach for interpreting genome-wide expression profiles. *Proc. Natl. Acad. Sci. U S A.* 102, 15545–15550.

Vafa, O., Wade, M., Kern, S., Beeche, M., Pandita, T.K., Hampton, G.M., and Wahl, G.M. (2002). c-Myc can induce DNA damage, increase reactive oxygen species, and mitigate p53 function: a mechanism for oncogene-induced genetic instability. *Mol. Cell.* 9, 1031–1044.

Vinogradova, M., Gehling, V.S., Gustafson, A., Arora, S., Tindell, C.A., Wilson, C., Williamson, K.E., Guler, G.D., Gangurde, P., Manieri, W., et al. (2016). An inhibitor of KDM5 demethylases reduces survival of drug-tolerant cancer cells. *Nat. Chem. Biol.* 12, 531–538.

Visvader, J.E. (2009). Keeping abreast of the mammary epithelial hierarchy and breast tumorigenesis. *Genes Dev.* 23, 2563–2577.

Weaver, V.M., Lelievre, S., Lakins, J.N., Chrenek, M.A., Jones, J.C., Giancotti, F., Werb, Z., and Bissell, M.J. (2002). beta4 integrin-dependent formation of polarized three-dimensional architecture confers resistance to apoptosis in normal and malignant mammary epithelium. *Cancer Cell* 2, 205–216.

Yu, C., Mannan, A.M., Yvone, G.M., Ross, K.N., Zhang, Y.L., Marton, M.A., Taylor, B.R., Crenshaw, A., Gould, J.Z., Tamayo, P., et al. (2016). High-throughput identification of genotype-specific cancer vulnerabilities in mixtures of barcoded tumor cell lines. *Nat. Biotechnol.* 34, 419–423.

STAR★METHODS

KEY RESOURCES TABLE

REAGENT or RESOURCE	SOURCE	IDENTIFIER
<b>Antibodies</b>		
Monoclonal mouse anti-cMyc antibody clone 9E10	SCBT	Cat # sc-40; RRID: AB_2857941
Monoclonal rabbit anti- Phospho-4E-BP1 antibody clone 236B4	CST	Cat # 2855S; RRID: AB_560835
Polyclonal rabbit anti-p-Akt antibody Clone Ser473	CST	Cat # 9271S; RRID: AB_329825
Monoclonal rabbit antibody anti- $\beta$ -Actin Clone 13E5	CST	Cat # 4970S; RRID: AB_2223172
Polyclonal rabbit anti-phospho-p70 S6 Kinase Clone Thr389	CST	Cat # 9205S; RRID: AB_330944
Phospho-Rb anti-rabbit antibody	CST	Cat # 9307S; RRID: AB_330015
Anti-rabbit IgG, HRP-linked Antibody	CST	RRID: AB_2099233
Anti-mouse IgG, HRP-linked Antibody	CST	RRID: AB_330924
<b>Biological Samples</b>		
Prostate cancer derived organoids (MSKCC)	Memorial Sloan Kettering Cancer Center	N/A
Breast cancer patient derived PDX material	Huntsman Cancer Institute	N/A
Human Genomic DNA: Female	Promega	G152A
<b>Chemicals, Peptides, and Recombinant Proteins</b>		
PBS	Corning	Cat # 21-040-CV
DMEM High Glucose	Life Technology	Cat # 11965118
Advanced DMEM/F12K	Life Technology	Cat # 12634010
Opti-MEM	Life Technology	Cat # 31985070
Trypsin 0.05%	Mediatech	Cat # 25-052-CI
Pen/Strep	Mediatech	Cat # 30-002-CI
Matrigel	Corning	Cat # 356253
Rat Tail Collagen	Corning	Cat # CB40236
Lipofectamine 2000	Life Technology	Cat # 11668019
Trypan Blue	Sigma Aldrich	Cat # T10282
Polybrene	SCBT	Cat # 134220
Estradiol	Sigma Aldrich	Cat # E2758
Dihydroxy testosterone	Sigma Aldrich	Cat # D-073-01 ml
Fulvestrant	Sigma Aldrich	Cat # I4409
Vinorelbine	Sigma Aldrich	Cat # V2264
Docetaxel	LC Laboratories	Cat # D-1000
Epirubicin	SelleckChem	Cat # E-8000
Carfilzomib	SelleckChem	Cat # S2853
EGF	Miltenyi Biotech	Cat # 130-093-825
FGF-10	R & D Systems	Cat # 345FG025
FGF-2	Peprtech	Cat # 100-18B
Nicotinamide	Acros Organics	Cat # AC128271000
A83-01	R & D Systems	Cat # 293910
SB-202190	Sigma Aldrich	Cat # S7067
Y-27632	Sigma Aldrich	Cat # Y0503
B27	Life Technology	Cat # 17504044
N-acetyl-L-Cysteine	Sigma Aldrich	Cat # A7250
Glutamax	Sigma Aldrich	Cat # 35050061

(Continued on next page)

**Continued**

REAGENT or RESOURCE	SOURCE	IDENTIFIER
HEPES	Sigma Aldrich	Cat # 15630080
Primocin	Invivogen	Cat # ANT-PM-2
JQ1	Provided by the lab of Dr. James Bradner (DFCI)	N/A
ZZ1-33 (aka THAL-SNS-032)	Provided by the lab of Dr. Nathanael Gray (DFCI)	N/A
NVP2	Provided by the lab of Dr. Nathanael Gray (DFCI)	N/A
SNS032	Provided by the lab of Dr. Nathanael Gray (DFCI)	N/A
FDA-approved oncology drugs (100 Compounds)	NCI-DTP	N/A
INK128	SelleckChem	Cat # S2811
Abemaciclib	SelleckChem	Cat # S7158
Vinblastine	Sigma Aldrich	Cat # V1377
Afatinib	SelleckChem	Cat # S1011
Zombie Aqua Dye	Biologend	Cat # 423102
Alexa Flour 647 cyt c dye	Biologend	Cat # 612310
Digitonin	Sigma Aldrich	Cat # D141
BIM/BID/PUMA Peptides	Provided by the lab of Dr. Anthony Letai (DFCI)	N/A
G-418	Life Technologies	Cat # 10131035
Blasticidine	Invivogen	Cat # ant-bl-1
Puromycin	Fisher Scientific	Cat # A1113803
Hygromycin	Life Technologies	Cat # 10687010
DMSO	Fisher Scientific	Cat # BP231100
Beetle Luciferin, Potassium Salt	Promega	Cat# E1605
SuperSignal West Dura Extended Duration Substrate	Life Technologies	Cat# 34076
Hygromycin B	Life Technologies	Cat# 10687010
Puromycin	Fisher Scientific	Cat# A1113803
Doxycycline hyclate	VWR	Cat# 89150-324

**Critical Commercial Assays**

CellTiter-Glo (CTG) assay	Promega	Cat # G7572
PCR-ELISA kit-Mycoplasma test	Roche Diagnostics	Cat # 11663925910
RealTime-Glo™ Annexin V Apoptosis and Necrosis Assay	Promega	Cat # JA1011
NADP/NADPH Quantitation Colorimetric Kit	Biovision	Cat # G9081
SYBR green power UP master mix	Life Technology	Cat# A25780
FxCycle PI/RNase staining solution	Life Technologies	Cat# F10797

**Deposited Data**

RNAseq	GEO	GEO: GSE162285
--------	-----	----------------

**Experimental Models: Cell Lines**

MCF7	ATCC	Cat # HTB-22
ZR75-1	ATCC	Cat # CRL-1500
Lenti-X-293T	ATCC	Cat # 632180
MDAMB-231	ATCC	Cat # HTB-26
Breast cancer patient derived organoids	This paper	N/A

**Experimental Models: Organisms/Strains**

Mouse: Crl:NU(NCr)-Foxn1nu	Charles River Laboratories	Charles River Laboratories Cat# 490
Mouse: NOD.Cg-Prkdc <sup>scid</sup>	The Jackson Laboratories	The Jackson Laboratories Cat# 005557

(Continued on next page)

**Continued**

REAGENT or RESOURCE	SOURCE	IDENTIFIER
<b>Oligonucleotides</b>		
CRISPR-Cas9 editing <i>MYC</i> _sgRNA1: ACAACGTCTTGAGCGCCAG	This paper	N/A
CRISPR-Cas9 editing <i>MYC</i> _sgRNA2: GCCGATTTCTACTGCGACG	This paper	N/A
CRISPR-Cas9 editing <i>OR10G2</i> : GGAGGCTTCTAGATTGGG	This paper	N/A
CRISPR-Cas9 editing <i>OR10G3</i> : GCTTAGCAGTCATGAGCACA	This paper	N/A
CRISPR-dCas9-KRAB interference <i>MYC_1</i> : CACCGAGGCAGAGGGAGCGAGCGGG	This paper	N/A
CRISPR-dCas9-KRAB interference <i>MYC_2</i> : CACCGCCCGGCTCTCCACCCTAGC	This paper	N/A
CRISPR-dCas9-KRAB interference <i>MYC_3</i> : CACCGGCAGCGCAGCTCTGCTCGCC	This paper	N/A
CRISPR-dCas9-KRAB interference <i>MYC_4</i> : CACCGGCTGTAGTAATCCAGCGAG	This paper	N/A
CRISPR-dCas9-KRAB interference <i>MYC_5</i> : CACCGGCGCTGCGGGCGTCCTGGAA	This paper	N/A
CRISPR-dCas9-KRAB interference <i>OR10G3</i> : CACCGGTGGATACGGAATTCCTGTC	This paper	N/A
CRISPR-dCas9-KRAB interference <i>OR6S1</i> : CACCGCAACAGAGTTCGTCCTGGCA	This paper	N/A
<b>Recombinant DNA</b>		
pLV[Exp]-EGFP/Neo-EFS>tTS/rtTA	Vector Builder	Cat # VB900088-2738UUK
pLV[Exp]-mCherry:T2A:Bsd-T RE>mCherry	Vector Builder	Cat # B181106-1162RRM
EF1a-Puro-WPRE-hU6-gRNA (gRNA Replaced with barcodes, Puro With EGFP)	Addgene	Addgene cat # 106280
pLX311-Cas9	Addgene	Addgene cat #118018
pHAGE TRE dCas9-KRAB	Addgene	Addgene (Plasmid #50917)
mCherry-luciferase vector	Provided by the lab of Dr. Andrew Kung (DFCI)	N/A
pQXCIP-Rspondin	Provided by the lab of Dr. Yu Chen (MSKCC)	N/A
pQXCIP-Noggin	Provided by the lab of Dr. Yu Chen (MSKCC)	N/A
pLV[Exp]-mCherry:T2A:Bsd-TRE>hMyc	Vector Builder	Cat # VB181106-1162RRM
<b>Software and Algorithms</b>		
FlowJo™ Software (for Windows) [software application] Version 10.7.1.	Becton, Dickinson and Company	N/A
GraphPad Prism V8 and V9	Graphpad	N/A
SPSS Statistics	IBM	N/A
Pycashier	<a href="https://github.com/DayiinMorgan/pycashier">https://github.com/DayiinMorgan/ pycashier</a>	N/A
Bioconductor R	<a href="http://github.com/aedin/barcodes">http://github.com/aedin/barcodes</a>	N/A

## RESOURCE AVAILABILITY

### Lead Contact

Further information and requests for resources and reagents should be directed to and will be fulfilled by the Lead Contact, Constantine S. Mitsiades ([constantine\\_mitsiades@dfci.harvard.edu](mailto:constantine_mitsiades@dfci.harvard.edu)).

### Materials Availability

The organoid models and plasmids generated in this study are available upon request to the Lead Contact.

### Data and Code Availability

The data retrieval, generation and analysis are described in the Methods section. Microarray and RNA-seq fold-change and counts tables are available as [Table S1](#) ( $\log_2$ FC in drug-refractory organoids and PDXs, *deseq* without beta correction), [Table S2](#) (read counts data from our organoids and PDX samples), and [Table S3](#) (extracted raw read counts from the BAM files provided from the Boroviak et al. study). The accession number for the raw sequencing data (RNA-seq) reported in this paper is GEO: GSE162285. RNA-seq from Boroviak et al., Scogniamiglio et al., and Bulut-Karslioglu et al., are available under the accession numbers ArrayExpress: E-MTAB-2958, GEO: GSE74337 and GEO: GSE81285, respectively. Custom scripts and pipelines used for data pre-processing are described in the method section.

## EXPERIMENTAL MODEL AND SUBJECT DETAILS

### Cell Lines

MDAMB-231, MCF-7, and ZR75-1 cell lines were purchased from ATCC. Lenti-X-293T cells were purchased from Clontech. The cells were routinely maintained in DMEM High Glucose, 4.5g/l D-Glucose, 110mg/l Sodium Pyruvate, 10% FBS, 10 i.u./ml penicillin and 10 $\mu$ g/ml streptomycin and passaged using trypsin. Authentication of the cell lines was performed by short tandem microsatellite repeat analysis. Before their use in experiments, the cells were tested for mycoplasma using a combined PCR-ELISA kit (Roche Diagnostics).

### Patient-Derived Models

The clinical characteristics of the patients are described in [Figure S1D](#). The PrCa patient-derived cells for the 3D-PDO models MSK-PCa1, MSK-PCa2, MSK-PCa3, MSK-PCa7 and PM154 were obtained at the Memorial Sloan Kettering Cancer Center and were expanded similarly to previous studies ([Gao et al., 2014](#)). The BrCa patient-derived samples HCI002, HCI003, HCI005, HCI007, HCI009 and HCI011 were initially engrafted as PDXs at the Huntsman Cancer Institute, as previously described ([DeRose et al., 2011](#)). Small PDX tissue fragments (1-2mm) were enzymatically processed for 1h at 37°C and the released floating malignant cells were collected by centrifugation, resuspended in matrigel, plated in 6-well plates and expanded as 3-D organoids, as previously described ([Gao et al., 2014](#)). The 3D-PDO cultures were maintained in Advanced DMEM/F12 supplemented with 3.151 ml/L D-glucose, 110 mg/L sodium pyruvate, EGF (50 ng/mL), FGF-10 (10 ng/mL), FGF-2 (1 ng/mL), Nicotinamide (10 mM), A83-01 (0.5  $\mu$ M), SB202190 (10  $\mu$ M), Y-27632 (10  $\mu$ M), B27 (1X), N-Acetyl-L-Cysteine (1.25 mM), GlutaMAX (2 mM), HEPES (10 mM), Primocin (0.5 $\mu$ g/ml), R-Spondin (10% v/v), Noggin (10% v/v), 0.1nM estradiol (for the BrCa 3D-PDOs only), 0.1nM DHT (for the PrCa 3D-PDOs only).

## METHOD DETAILS

### Reagents

PBS (Corning), DMEM High Glucose (Life Technologies), Advanced DMEM/F12 (Life Technologies), Opti-MEM (Life Technologies), trypsin 0.05% (Mediatech), penicillin/streptomycin 1X (Mediatech), Matrigel (Corning), rat tail collagen (Corning), Lipofectamine 2000 (Life Technologies), Trypan blue (Sigma Aldrich), polybrene (Santa Cruz Biotechnology), estradiol (Sigma Aldrich), dehydrotestosterone (Sigma Aldrich), fulvestrant (Sigma Aldrich), vinorelbine (Sigma Aldrich), docetaxel (LC Laboratories), epirubicin (SelleckChem), carfilzomib (SelleckChem), EGF (Miltenyi Biotec), FGF-10 (R & D Systems), FGF-2 (Peprotech), nicotinamide (Acros Organics), A83-01 (R & D Systems), SB202190 (Sigma Aldrich), Y-27632 (Sigma Aldrich), B27 (Life Technologies), N-Acetyl-L-Cysteine (Sigma Aldrich), Glutamax (Life Technologies), HEPES (Life Technologies), Primocin (Invivogen), monoclonal mouse anti-cMyc antibody clone N-262 (Santa Cruz Bio.). R-spondin and Noggin were generated by collection of conditioned media from HEK293T cells transfected with the respective expression plasmids, as previously described ([Gao et al., 2014](#)). BET inhibitor JQ1 and CDK9 degrader ZZ1-33 (also referred to as THAL-SNS-032) and inhibitors NVP2 and SNS032 were provided by the laboratories of Drs. Nathanael Gray and James Bradner. The chemical library panel of FDA-approved oncology drugs (100 compounds) was a kind gift from the Developmental Therapeutics Program of the NCI.

### 3D Cultures

For simplicity, in this manuscript we use the term “organoids” to refer to multicellular 3-D structures formed in gels by cancer cells originating from either established cell lines or patient-derived tumors. We recognize that in the literature, 3D structures formed by cancer cell lines are often referred to as “spheroids”, while the term “organoid” is frequently used, especially in recent years,

for material that was recently derived from patients. The use of the term “organoid” for 3D cultures of both cell line and patient-derived samples also reflects that in this study and others (i) many cell lines do not form typical “spheroid” structures in 3D, and therefore the term “organoid” is more reflective and inclusive; (ii) other cell lines form in 3D cultures structures that are indistinguishable with those from patient-derived “organoids”.

The cells were suspended in 80% matrigel as previously described (Dhimolea et al., 2010). The gels were cast in either 12-well (for histological and molecular analyses) or multi-well plates (for cell viability assays; described below). The gels were incubated for 1h at 37°C to allow for solidification, supplemented with medium, and used for further downstream applications (see other sections of STAR Methods). To extract the cells from 3-D organoids, the gels were first disrupted mechanically in cold PBS; next, the organoids were isolated by centrifugation and incubated in trypsin for 20-30 min to generate single-cell solution.

### Whole Exome Sequence Analysis of Patient-Derived Cancer Models

A total of 14 paired-end sequencing samples (Illumina HiSeq 2000) were processed for matched analysis of prostate cancer primary tumors, xenografts and organoids for the models MSK-PCa1, MSK-PCa2, MSK-PCa3 and MSK-PCa7. A total of 31 paired-end sequencing samples (Illumina HiSeq 2000) were processed for matched analysis of breast cancer primary tumors, xenograft and organoids for the models HCI-002, HCI-003, HCI-005, HCI-007, HCI-009, and HCI-011. The exome-seq data was generated using Agilent Sureselect per manufacturer’s instructions. We aligned reads to the human genome (hg19) using the BWA (Burrows-Wheeler alignment) application (Li and Durbin, 2009). We applied the Picard and the GATK (GenomeAnalysisTK-3.6) tools (McKenna et al., 2010) for processing BAM files of aligned reads generated by the bwa application for each sample. For the analysis we followed the GATK best practices recommendations. In detail, reads in the BAM files were sorted and duplicated reads were removed. The alignments were realigned around indels and quality scores were recalibrated based on GATK. We processed BAM files using the picard (picard-1.138) tools ReorderSam, SortSam, AddOrReplaceReadGroups and MarkDuplicates. The alignment recalibration was performed using the GATK tools RealignerTargetCreator, IndelRealigner, BaseRecalibrator and PrintReads. Known SNP for the base recalibration were defined based on the NCBI dbSNP database (dbsnp\_138.hg19.vcf). We used samtools for the indexing of BAM files. The identification of single nucleotide polymorphisms (SNPs) was performed based on GATK tools UnifiedGenotyper, VariantFiltration and Mutect2. For Mutect2 we filter out known human variants dbSNP138 and retain SNPs of known cancer associated mutations from the COSMIC database. Unreported SNPs were annotated using SnpEff and variantAnnotator from GATK.

Copy number variation was estimated based on GATK4 tools PadTargets, CalculateTargetCoverage, CombineReadCounts, CreatePanelOfNormals, NormalizeSomaticReadCounts, PerformSegmentation and CallSegments. The panel of normal controls (PON) were generated from matched blood samples. For the prostate cancer samples we used as normal controls 3 paired-end sequencing samples (MSK-PCa1\_BM1, MSK-PCa2\_BM5 and MSK-PCa3\_ST1). For the breast cancer samples normal controls we used 3 paired-end sequencing samples (HCI-002\_0900570-B, HCI-003\_0903293-B, HCI-005\_1007496-B). The sequence processing procedures were performed on the Orchestra High Performance Compute Cluster (HPC) at Harvard Medical School. The Orchestra HPC NIH supported shared facility is partially provided through grant NCR11S10RR028832-01. These analyses were conducted to confirm the concordance of genetic features between our pre-clinical models (xenografts and organoids) and their respective original patient tumors (data not shown).

### Persist vs Vehicle Exome Sequencing Analysis

The fastq files were processed as described above and alignments were recalibrated based on GATK best practices. The identification of single nucleotide polymorphisms (SNPs) was performed based on GATK tools Mutect2 and FilterMutectCalls using commercially-available anonymized normal female DNA as comparator (Promega). SNPs were annotated using Oncotator (Ramos et al., 2015) and we considered only non-synonymous SNPs causing a change in protein sequence. We used bam-readcount (<https://github.com/genome/bam-readcount>) to extract the nucleotide frequencies for each called mutation from the “PASS” filtered mutect2 output. The Tumor allele was defined from Oncotator annotated SNP calls and we extracted the total readcount and the tumor allele readcount from the respective BAM alignment files (Persist vs Vehicle) using bam-readcount. The tumor allele frequency was estimated by dividing the number of reads encoding the tumor allele by the total number of reads for the respective loci. In order to exclude low read coverage loci we considered only loci for the HCI002 with a 50x coverage in each of both the Persist vs untreated vehicle sample. For the MDAMB-231 Persist vs and for the untreated vehicle sample we considered a 200x read coverage in the loci in each of both samples.

### Cell Viability Assays

Cell lines MCF-7, ZR-75-1, MDAMB-231, and 3D-PDO models HCI002, HCI003, HCI007, HCI009, HCI011, MSK-PCa1, MSK-PCa2, MSK-PCa3, MSK-PCa7 and PMI154 were stably transfected with lentiviral vectors expressing the luciferase gene, which allows the use of the emitted bioluminescence to longitudinally and non-disruptively measure cancer cell viability, as previously described (McMillin et al., 2012). The effects of chemotherapeutics, JQ1 and CDK9 inhibitors in cell lines or patient-derived organoids were also confirmed using CellTiter-Glo (CTG) assay (Promega) cell viability assays following manufacturer’s instructions. The assay results (quadruplicates) were analyzed in Excel and plotted in GraphPad Prism (error bars represent standard error of the mean). Two *in vitro* culture configurations were applied in these studies:

### 2-D Culture Cell Viability Assays

The cells were seeded into 384-well plates ( $500\text{-}2\times 10^3$  cells/well) in supplemented media ( $50\ \mu\text{L}$ – $100\ \mu\text{L}$ /well) and incubated for 24h prior to addition of compound/s at indicated concentrations.

### 3-D Organoids Cell Viability Assays

The cells were plated in Matrigel similarly to single-cell format. After plating, the cells were allowed to grow for 7–10 days into 3-D organoids. Once the organoid structures were formed (confirmed by microscope observation), the medium was replenished, and the organoids were incubated for 24 more hours before adding the compound(s) at indicated concentrations.

To confirm that the cytotoxic effect of the tested drugs is not affected by the properties of Matrigel, we compared the activity of common chemotherapeutics against tumor cells grown as 2D monolayers, single-cells in Matrigel (i.e. exposed to the drug before forming 3D organoids) and as organoids in Matrigel (Figure S1A and S1B). During prolonged drug-response assays the medium and tested compounds were replenished at regular intervals. At each indicated time point (1–21 days) either luciferin (for the luciferase-positive cells; concentration per manufacturer's instructions) or CTG reagent (per manufacturer's instructions) was added to each well, and the plates were read using a microplate reader (BioTek Synergy 2). The linearity of bioluminescence assay in 3-D cultures was estimated by measuring the signal of known cell numbers in 3-D cultures (data not shown).

### EDL Organoids Regrowth Suppression Experiment

MDAMB-231 3-D organoids were exposed to the indicated chemotherapeutic agents for 96h to generate persister organoids (phenotypically and morphologically similar to Figures 1B and 1D, respectively); next, the gels were washed in cold PBS and the persister organoids were extracted and re-embedded in new gels and incubated in the presence of JQ1 (200nM), INK128 (100nM) or DMSO-control. The MDAMB-231 cells were extracted from the newly-formed gels at indicated time points using cold PBS and, when necessary, brief incubation with trypsin at  $37^\circ\text{C}$  to generate single-cell solution. The growth rates of persister organoids after drug washout was estimated by cell counting (Countess automated cell counter) at indicated time points. Cell counting measurements were also confirmed by bioluminescence-based measurements.

### PRISM-based Phenotypic Studies in Pools of Barcoded Cancer Cell Lines

PRISM is a method that allows pooled screening of mixtures of cancer cell lines by labeling each cell line with a distinct 24-nucleotide barcode and has been previously described in detail (Yu et al., 2016). Briefly, we used a collection of adherent cancer cell lines that stably expressed DNA barcode sequences with limited sequence homology to the human genome. For the 2-D cultures, the cells were seeded in 25cm flasks ( $100\times 10^3$ /flask in experimental triplicates) and incubated in supplemented medium for 24h before adding docetaxel (100nM) or DMSO-control. For the 3-D cultures, the cells were suspended in matrigel and dispensed in 10cm dishes ( $100\times 10^3$  in 1ml matrigel/dish); let at  $37^\circ\text{C}$  for 30 min to solidify and supplemented with culture medium. The gels were incubated at  $37^\circ\text{C}$  for 8 days to allow for 3-D organoid structures formation (confirmed by microscope observation), followed by medium replenishment and addition of docetaxel (100nM) or DMSO-control the next day. Both 2-D and 3-D cultures were harvested 5, 10 and 15 days after the start of treatment. The cellular DNA was isolated using standard DNA extraction kit (Qiagen) and sequenced to estimate the copies of the specific barcodes corresponding to distinct cell lines, as previously described (Yu et al., 2016). The comparison of the normalized counts for each barcode between treated conditions and the respective time-point DMSO-controls, was used to estimate the docetaxel-induced reduction of viability for 253 cell lines that grew in 3D conditions.

### Barcode-Mediated Clonal Tracking Experiment

The barcoded sgRNA library was generated as previously described (Al'Khafaji et al., 2019). Briefly, the Crop-seq-opti vector (available from Addgene 106280) was modified by replacing the Puro resistance marker with Vex-GFP using restriction cloning. We cloned a gRNA library on the modified Crop-seq-opti\_Vex vector using the BsmBI restriction site. The double stranded 58 bp barcoded gRNA insert library was generated by performing a PCR extension reaction with the following primer oligos:

N20\_gRNA GAGCCTCGTCTCCACCGNNNNNNNNNNNNNNNNNNNGTTTTGAGACGCATGCTGCA  
and gRNA\_RevExt TGCAGCATGCGTCTCAAAC

as follows:  $98^\circ\text{C}$  for 2 min,  $10\times$  ( $65^\circ\text{C}$  for 30 s,  $72^\circ\text{C}$  for 10s),  $72^\circ\text{C}$  for 2 min, hold at  $4^\circ\text{C}$ . The double stranded barcode-sgRNA oligo was purified using a QIAquick PCR Purification Kit (Qiagen, #28104). The double-stranded product contains two BsmBI sites that, upon digestion, generate complimentary overhangs for ligation into the Crop-seq-opti\_Vex. Assembling of the double-stranded barcode-sgRNA insert into the Crop-seq-opti\_Vex vector was done using a Golden Gate assembly reaction at a molar ratio of 1:5 and cycled  $100\times$  ( $42^\circ\text{C}$  for 2 min and  $16^\circ\text{C}$  for 5 min). The assembled plasmid was then purified using the DNA Clean & Concentrator™ kit (Zymo, #D4033) and used to transform Endura electrocompetent cells (Lucigen, #60242-2). Transformed bacteria were inoculated in 500 ml 2xYT medium containing  $100\ \mu\text{g}/\text{ml}$  carbenicillin incubated overnight at  $30^\circ\text{C}$ . Plasmid DNA was extracted using a Qiagen Plasmid Plus Midi Kit (Qiagen #12943).

Lentiviral preps were generated by transfecting Lenti-X 293T cells with the Crop-seq barcode library and packaging plasmids psPAX2 and MD2.G. The MDAMB-231 cells were transfected with the generated viral preps at low MOI ( $\sim 10\%$  transfection efficiency; assessed by flow cytometry) to ensure that most cells receive one single barcode; flow cytometry analysis indicated 6% transfection rate. Approximately 125000 EGFP+ cells (roughly representing equivalent number of barcodes) were collected by flow cytometry and expanded in culture. Prior to inoculation in animals, a pellet of 2 million cells was frozen to assess the baseline distribution of barcodes (T0). The rest of the cells were inoculated s.c. in 15 SCID mice (2 million cells per animal). When tumors

reached  $\sim 50\text{-}100\text{mm}^3$  the animals were randomized into 3 groups and treated with docetaxel (15mg/kg), epirubicin (3mg/kg) or DMSO control 3 times per week. The dose of docetaxel was lowered to 10mg/kg after the second week to decrease systemic toxicity. After 4 weeks of treatment all tumors were harvested and genomic DNA was extracted. The gDNA was amplified by PCR (2  $\mu\text{g}$  gDNA per 25  $\mu\text{L}$  reaction; 5 reactions per harvested tumor) using Q5 PCR master mix and thermal cycles: 98°C for 2 min, 22x (98°C 10 s, 65°C 30 s, 72°C 15 s), 72°C 2 min, 4°C indefinitely. The PCR product was purified using the Ampure cleanup kit and sequenced using the Illumina NextSeq platform.

### Analysis of Clonal Composition Using Sequenced Barcodes

Counts of expressed barcode tags were extracted from FASTQ files using Pycashier (<https://github.com/DaylinMorgan/pycashier>), an extension of Cashier (developed by Russell Durrett). Pycashier is a wrapper that uses cutadapt to identify and remove flanking adapter sequences and starcode (v1.3) to perform fast minimum levenshtein clustering. FASTQ Files were uncompressed and renamed in order to run Pycashier. Default parameters were used including Pread quality filtering of 30, levenshtein clustering with a ratio 3, distance 1 and filtering reads that have counts less than 10. A cut-off of 10 was confirmed as an appropriate threshold in a cumulative plot of barcode frequencies as described in Bystrykh L et al., On a cumulative frequency scale, the curve noticeably bent at the turning point, indicating the change from high frequencies (true barcodes) to very low frequencies of barcodes (false) close to 10. The experiment was run in 2 batches, the second batch (D3-5, E1-5) were grown for longer (2-3 days) in culture. There was no difference in the median count between batches, but there was a difference in library depth (colSums) and upper quantiles. Quantile normalization (R package preprocessCore::normalize.quantiles) was applied to adjust the batch effect and read counts were adjusted by the median ratio method (Li et al., 2014). Specifically, the adjusted read count  $x$  is calculated as the rounded value of  $x/s$ , where  $s$  is the size factor in experiment  $j$  and computed as the median of all size factors calculated from individual sgRNA read counts. In total 168,852 barcodes were observed in one or more samples. The greatest barcode diversity ( $n=134,488$ ) was in T0 whereas a mean of 30,889, 22,806 and 30,752 barcodes were detected in vehicle (V), Dox (D) and Epi (E) treated animals respectively. In differential barcode analysis, barcode with 2 or fewer observations in vehicle, or in either treatment animal (min(D,E)) were excluded. Non-parametric Rank Product (geometric mean rank) analysis (Breitling et al., 2004) was used to identify barcodes that were differentially enriched in treatment compared to vehicle. P values were corrected for multiple testing using the False Discovery Rate (FDR, (Benjamini and Hochberg, 1995)). Additionally differential barcode analysis using a negative binomial model was applied as described by Li et al (Li et al., 2014). Linear regression analysis of barcodes was performed using Bioconductor packages voom, limma and p value were adjusted for multiple testing using the FDR. Wilcox signed rank test was performed on barcode alpha (Shannon) and Beta (Bray Curtis) diversity indices, calculated using the R package functions `vegan::vegdist`, `vegan::betadisper`. Shannon index assessed the barcode diversity within an observation, whereas Bray Curtis indices measure the pairwise dissimilarity between observations (samples). The Bray Curtis index is 0 if the two observations share all the same barcodes and 1 they don't share any common barcodes. Tukey Honest significant differences' test was also used to examine the overlap in confidence intervals on the differences between the means of Bray Curtis dissimilarity indices. Bioconductor R version 4.0.2 was used in all statistical analyses and code is available on github (<http://github.com/aedin/barcodes>).

### NADPH/NADP Measurement Assay

The cells were seeded as 2-D cultures in 10 cm dishes ( $1 \times 10^6$  cells/dish). JQ1 was added the next day, followed by addition of epirubicin or DMSO-control 4h later. The cells were harvested after 12h by scrapping in cold cell recovery solution, followed by centrifugation and pellet storage at  $-80^\circ\text{C}$ . The cellular pellets from 2-D and 3-D cultures were processed for NADP/NADPH measurement using the NADP/NADPH Quantitation Colorimetric Kit (BioVision), according to manufacturer's instructions. An increased NADP/NADPH ratio is indicative of higher redox stress levels.

### Apoptosis Assay

The rate of cell apoptosis in 2D and 3D cultures was estimated by luminescence measurement, using the RealTime-Glo™ Annexin V Apoptosis assay (Promega, Madison, WI) following the manufacturer's instructions. Briefly, the cells were incubated with two annexin V fusion proteins (Annexin V-LgBiT and Annexin V-SmBiT) which contain complementary subunits of NanoBiT® Luciferase; and a time-released luciferin. The increased cell surface levels of membrane phosphatidylserine in apoptotic cells brings the Annexin V-LgBiT and Annexin V-SmBiT luciferase subunits into complementing proximity, which is reflected by the strength of bioluminescence signal emitted in culture (quadruplicate measurements per experimental condition).

### BH3 Profiling

Flow cytometry-based BH3 profiling was performed as previously described (Ryan et al., 2016). Briefly, cells were stained with Zombie Aqua Dye (Biolegend, #423101) to assess viability, followed by permeabilization, incubation for 90 minutes with the peptides BIM and BID, and staining with cytochrome C-Alexa Fluor 488 (Biolegend, #612308). Flow cytometry analysis was performed on a LSRFortessa X-20 machine (BD Biosciences) and the results analyzed on the FlowJo software. The percentage of cytochrome C release in persister organoids vs. control was calculated based on average of the Mean, Geometric Mean, or Median of Fluorescence Intensity (MFI) of the Cytochrome C -Alexa Fluor 488 staining normalized to the respective values of the positive and negative controls in the same sample (respectively cells exposed to buffer or 25 $\mu\text{M}$  alamethicin). For the MYC-KD and JQ1-treated cells, the percentage of cytochrome C release (duplicates) was calculated based on the Median of Fluorescence Intensity (MFI) of the Cytochrome C-Alexa Fluor 488 staining normalized to the respective values of the positive and negative controls in the same sample (respectively

cells exposed to buffer or 25 $\mu$ M alamethicin). Apoptotic priming was visualized in graphs using the average percentage of cytochrome C release  $\pm$  SEM of duplicates. The experiments were repeated 2 times to ensure consistency of the data.

### Cell Cycle Analyses

Cell cycle analysis was performed in cells from 3D cultures. The gels were initially disrupted mechanically using cold PBS. The 3-D organoids were isolated by centrifugation and incubated with trypsin for 20 min at 37°C to generate single-cell suspensions. The cells isolated from 3D cultures were stained using the FxCycle™ PI/RNase Staining Solution (Thermo Fisher) according to manufacturer's instructions and analyzed by flow cytometry.

### Histological Analyses

Cells suspended in matrigel were cast in 12-well plates (1.5 ml/well) and the gels were let to solidify for 1h at 37°C. After gel solidification, the 3-D cultures were supplemented with medium and incubated for 7-8 days to allow for organoid formation. Gels were then extracted from the culture vessel and fixed in 10% formalin. Subsequently, the gels were processed for paraffin embedding and immunohistochemistry (slide sections), as previously described (Dhimolea et al., 2010, 2020). Tumor tissues were fixed in 10% formalin and processed for immunohistochemistry following standard protocols.

### Western Blot

Cell lysates were analyzed using 7% NuPage Tris-Acetate gels (Invitrogen) according to manufacturers' instructions and transferred to a nitrocellulose membrane. The membranes were incubated overnight at 4°C with primary antibody for the respective target (see [Key Resources Table](#)), followed by incubation with the respective secondary anti-mouse or anti-rabbit HRP-linked antibody at room temperature for 1 h. The protein bands were visualized using chemiluminescence solution (RPN2232; GE Healthcare).

### CRISPR-Cas9 Mediated MYC Gene Knockout

Lentiviral particles were generated as described above. MDAMB-231 cells were first transduced with the lentiviral construct pLX311-Cas9 to generate MDAMB-231/Cas9+ cells. Next, two target sgRNA sequences for *MYC*, as well one target sequence for each of the olfactory receptor genes *OR10G2* or *OR10G3* (used as controls, given the biological inertness of these genes in epithelial cancers), were cloned into the Lenti X CRISPR-Cas9 (Clontech) according to manufacturer's instructions. The sgRNA target sequences are as follows:

*MYC*\_sgRNA1: ACAACGTCTTGGAGCGCCAG  
*MYC*\_sgRNA2: GCCGATTTCTACTGCGACG  
*OR10G2*: GGAGGCTTCTTAGATTTGGG  
*OR10G3*: GCTTAGCAGTCATGAGCACA

MDAMB-231/Cas9+ cells were incubated for 16h in cell medium, and viral prep at 2:1 ratio (polybrene was added at 8 $\mu$ g/ml concentration). After the end of the incubation with the viral preps, cells were washed and incubated for additional 24h. Next, the transduced cells were transferred to 6-well plates and selected with hygromycin (1 mg/ml) for 72h. The effect of chemotherapeutics on the transduced cells was assessed by two cell viability assays: a) Transduced cells were plated in 384-well plate and treated the next day with chemotherapeutics at the indicated doses. Cell viability was assessed by CTG as described in previous section. b) The transduced cells were exposed to chemotherapeutics at concentrations and durations indicated in the respective experiments. Next, the cells were harvested using trypsin and incubated with 0.4% trypan blue for 5 min; the number of dead and live cells was estimated using the Countess II FL automated cell counter.

### CRISPR-interference Mediated MYC Gene Knockdown

We performed the CRISPR-interference experiments similar to previously described protocols (Kearns et al., 2014). The plasmid construct pHAGE TRE dCas9-KRAB expressing the tet-regulatable dCas9-KRAB was obtained from Addgene (Plasmid #50917) and used to generate lentiviral particles with Lenti-X 293T cells and packaging plasmids psPAX2 and MD2.G. The plasmid was introduced in MDAMB-231 cells via lentiviral transduction and the cells expressing the tet-inducible dCas9-KRAB vector were selected using G418 (1 mg/ml). The following sense (and respective antisense) sgRNA sequences for CRISPR interference against *MYC* or olfactory receptor genes were generated:

*MYC*\_1: AGGCAGAGGGAGCGAGCGGG  
*MYC*\_2: CCCGGCTCTTCCACCCTAGC  
*MYC*\_3: GCAGCGCAGCTCTGCTCGCC  
*MYC*\_4: GCTGTAGTAATTCCAGCGAG  
*MYC*\_5: GCGCTGCGGGCGTCTCTGGGAA  
*OR10G3*: GTGGATACGGAATTCCTGTC  
*OR6S1*: CAACAGAGTTCGTCTGGCA

and subsequently cloned into the BsmBI site of plasmid pXPR\_050. Next, the MDAMB-231 cells expressing the doxycycline-inducible dCas9-KRAB vector were lentivirally transduced with the sgRNA-expressing constructs and selected using puromycin

(1  $\mu$ g/ml). Doxycycline-induced dCas9 expression was titrated by western blot. Gene knockdown was also assessed by western blot for target protein. Exposure to 2 $\mu$ g/ml doxycycline induced Myc downregulation within 3 days. Examples with sgRNA\_MYC\_2, sgRNA\_MYC\_3 and sgRNA\_MYC\_4 are shown (Figure S6A).

### Myc Overexpression

Doxycycline-mediated induction of Myc was enabled by first transducing MDAMB-231 or MCF7 cells with the lentiviral vectors pLV[Exp]-EGFP/Neo-EFS>tTS/rtTA, and next with pLV[Exp]-mCherry:T2A:Bsd-TRE>hMyc or as control pLV[Exp]-mCherry:T2A:Bsd-TRE>mCherry; followed by selection with the respective antibiotics. The lentiviral vectors were purchased from VectorBuilder.

### Animal Studies

The *in vivo* experiments were conducted in accordance with the guidelines of the DFCI Institutional Animal Care and Use Committee. For phenotypic and molecular profiling studies, MSK-PCa1 or HCl003 patient-derived organoid cells or MDAMB-231 cells were suspended in medium containing 20% matrigel and injected subcutaneously in the flank of NOD.Cg-Prkdc<sup>scid</sup> mice (2x10<sup>6</sup> cells/injection). The mice bearing MSK-PCa1 or HCl003 tumors were implanted with dihydrotestosterone or estradiol pellets, respectively. When the average tumor diameter reached approximately 1 cm, the mice were separated into treatment vs. control groups as indicated and treated with either vinblastine/control (2 mg/kg, weekly i.v. injections, for MSK-PCa1 PDX), afatinib/control (25 mg/kg by daily oral gavage, for the HCl003 PDX), docetaxel (5 mg/kg 3 times per week) or/and NVP2 (1 mg/kg 3 times per week) for the MDAMB-231 xenografts. Tumor growth or response to treatment was monitored by caliper measurements or by *in vivo* bioluminescence measurements. Residual drug-persistent tumors were collected after 2-4 weeks, at the plateau phase of tumor burden curves.

### Proteomic Analysis (Reverse Phase Protein Analysis, RPPA)

RPPA analyses were conducted by the Functional Proteomics RPPA Core facility (Houston, TX), which is supported by MD Anderson Cancer Center Support Grant # 5 P30 CA016672-40. We examined the expression levels of 303 proteins in HCl009 and HCl011 3D-PDO samples (isolated as described above) treated with either DMSO-control or docetaxel 100nM (experimental duplicates). Lysates of these protein samples were processed by the Core based on protocols and procedures outlined on the website of the facility (<https://www.mdanderson.org/research/research-resources/core-facilities/functional-proteomics-rppa-core/rppa-process.html>). Antibody array signal reads from replicates were averaged for each protein. The resulting matrix of RPPA data was provided as log-transformed linear normalized, linear normalized, and normalized median centered data.

### Sample Collection and Gene Expression Analysis

The cells in 2-D cultures were collected by scraping in cold cell recovery solution, pelleted by centrifugation and stored at -80°C. The 3-D gels were disrupted mechanically using cold cell recovery solution and 3-D organoids were collected by centrifugation and stored at -80°C. The gels of most 3-D PDO models were collected 10-12 days after drug exposure. For the washout studies, the gels of 3-D PDO models HCl009 and HCl011 were collected 5 days after drug exposure and 5 days post drug washout (after 12 days total drug exposure). The gels of 3-D PDO MSK-PCa7 were collected 12 days after drug exposure and 5 days after drug washout. The RNA was isolated using Qiagen RNA isolation kit. The RNA isolated from 3D-PDOs and MDAMB-231 organoids (experimental triplicates) treated with vehicle, docetaxel, or afatinib was supplemented with ERCC RNA spike-in mix to adjust for the cell number, and subsequently analyzed by RNA sequencing using Illumina NextSeq 500 Next Gen at the Molecular Biology Core Facility (Dana-Farber Cancer Institute). We performed differential gene expression analysis for the RNA-seq data using the bioconductor DEseq2 package (Love et al., 2014).

### Public Datasets Used

The molecular profiles of bulk post-treatment residual patient tumors were obtained from datasets GEO: GSE87455 (Kimbung et al., 2018), GEO: GSE32603 (Magbanua et al., 2015), GEO: GSE43816 (Gruosso et al., 2016) and GEO: GSE32072 (Gonzalez-Angulo et al., 2012). The PROMIX trial dataset GEO: GSE87455 (which is the largest of these clinical datasets) was analyzed at individual patient level using the residual tumor samples collected after 2 cycles of chemotherapy (69 patients; e.g. Figure 3G) or after 6 cycles of chemotherapy, at surgery (58 patients), versus the respective baseline samples. A similar analysis of I-SPY1 trial dataset GEO: GSE32603 (42 patients) at patient level is depicted in Figure S5D. For each patient in the PROMIX trial we examined the correlation between the changes in transcript levels (residual vs baseline tumors) with the respective transcript changes (residual vs baseline) for each of the other patients of the same trial, or with the transcript changes observed in our pre-clinical models of treatment persistence (versus baseline). This analysis intended to examine whether the correlation between the adaptive transcriptional changes in treatment-persistent residual pre-clinical models and clinical samples is similar to the correlation observed between the individual patients (Figure 1F).

The molecular profiles of single cell post-treatment residual patient tumors (versus their baseline) were obtained from dataset SRA: SRP114962 (Kim et al., 2018). For the single-cell RNAseq profile, sample annotations were imported from the public dataset. Raw fastq files were downloaded from ENA. Adapter and quality trimming was performed using BBDMap (v.38.73), and single end reads were aligned against the GENCODE v.32 hg38 transcriptome using salmon (v.1.0.0). In cases where read pairs were present, only read 2 was used. Further processing was performed in R/Bioconductor. Salmon quantification results were imported with tximport, using the transcripts to gene symbol mappings generated from the GENCODE gtf file. Analysis was performed using

Seurat after normalization with *SCTransform*. Signature scores were calculated by the *SingleCellSignatureScorer* module of the *SingleCellSignatureExplorer* using counts obtained from the Seurat *SCTransform* function. For plotting the single-cell copy numbers (Figure 3C) we used the processed data matrix of long integer copy numbers from the whole genome sequencing data provided by the authors of the paper (Kim et al., 2018). Figures 1G–1I and Figures 3C and 3D depict the single cell RNA profile of patient 615 from that study.

The transcriptional profiles of mouse embryonic stages were obtained from the Boroviak et al. (Boroviak et al., 2015) dataset with EBI ArrayExpress (Kolesnikov et al., 2015) accession ArrayExpress: E-MTAB-2958. We generated a read count matrix from the provided BAM files using feature counts from the *subread* package (version 1.5.2) (Liao et al., 2014). For the gene level feature counts, we used the GTF annotation file from Cell Ranger 10X Genomics (version cellranger-mm10-1.2.0; <http://www.10xgenomics.com>). Mouse Ensemble gene identifiers were mapped to MGI Gene symbols and retrieved using the Bioconductor *biomaRt* package (Durinck et al., 2009). The transcriptional profile of a second mouse embryonic diapause dataset (GEO: GSE143494) was used to confirm the results obtained with the Boroviak et al. dataset (Figure S5E).

### Human to Mouse Orthologous Gene Mapping

We retrieved orthology mapping of mouse gene symbols to human gene symbols from the MGI database (Blake et al., 2017). The mapping was extracted from the report HOM\_MouseHumanSequence.rpt and is available at <ftp://ftp.informatics.jax.org> (accessed August 2017). When multiple human genes mapped to a single mouse gene symbol, we assigned the expression value of corresponding mouse gene symbol for each human gene symbol. Mouse gene symbols without a human mapped gene symbol were excluded from the analysis.

### Gene Set Enrichment Analysis (GSEA)

The GSEA analyses were performed using the GSEA software (Subramanian et al., 2005) version 3.0 (gsea-3.0.jar) based on the pre-ranked option. For each differential gene expression analysis we use the per gene fold-change for gene ranking (concordant results observed with other ranking parameters, e.g. FDR). For the visualizations we use the GSEA enrichment scores (ES) and the gene set size normalized enrichment scores (NES). For gene set enrichment plots in Figures 1E, 6G, and 7H we used the top 1000 genes with  $FDR < 0.05$  in persistor HC1002 model and the mouse embryonic diapause (Boroviak dataset (Boroviak et al., 2015)); concordant results were observed with other cutoffs.

### Embryonic Diapause-like (EDL) Signature Score, EDL Proneness Signature and Survival Analysis

The EDL score was estimated by the Spearman correlation coefficient for the GSEA enrichment scores of all terms with nominal significance in Embryonic Diapause (DIA vs E4.5 EPI; Boroviak dataset) compared to the respective GSEA enrichment scores estimated for the comparison of each of the organoid, PDX and patient derived samples (e.g. Treatment vs Baseline, Surgery vs Baseline) versus their respective baselines. We performed GSEA using the Molecular Signature Database (MSigDB v6.2) (Subramanian et al., 2005), the Gene Ontology GO database (Ashburner et al., 2000) and the ConsensusPathDB-human database (CPDB) (Kamburov et al., 2013). The GO gene set collection was extracted from the bioconductor org.Hs.eg.db package (Carlson et al., 2016) for the biological process, cellular component and molecular function domain.

Based on the intensity of EDL signature score in residual tumors, patients of the PROMIX or ISPY datasets were classified into EDL-high and EDL-low groups, to compare the transcriptional profiles of baseline tumors between these two groups in each dataset and derive a transcriptional signature of the proneness of baseline tumors to eventually develop EDL during treatment. An EDL-proneness signature based on the top 50 upregulated and top 50 downregulated genes in baseline tumors of EDL-high vs. EDL-low groups from the PROMIX or I-SPY datasets were then used to stratify BrCa patients of the METABRIC dataset and examine potential differences in clinical outcome between the patients with high vs. low EDL-proneness signature. Concordant results were obtained with EDL-proneness signatures generated based on different numbers of up- or down-regulated genes in baseline tumors of EDL-high vs. EDL-low groups and different cutoffs to stratify patients according to EDL proneness score (data not shown).

### Pairwise 2D GO Analysis

We defined the gene sets from the Gene Ontology database (Ashburner et al., 2000) that were provided by the bioconductor org.Hs.eg.db package and from the comprehensive pathway and gene set collection provided from the ConsensusPathDB-human database (CPDB) (Kamburov et al., 2013). We implemented the 2D annotation enrichment analysis in the script language R as previously described (Cox and Mann, 2012). We performed Hotelling's  $T^2$  test for each gene set using the Manova function in R. We considered a total of about 8816 GO-terms and 3110 CPDB-pathways that are associated with at least 10 genes represented in a respective gene expression dataset. For each term we tested the null-hypothesis whether the composite mean value of the gene ranks of a given gene set from the two datasets is larger or smaller than the global composite mean value of the genes that are not members of the respective gene sets for the two datasets. In order to consider multiple hypothesis testing, we applied the FDR multiple testing correction procedure as previously defined (Benjamini and Hochberg, 1995). As described in Cox et al. (Cox and Mann, 2012), we employed a position score for each gene set for the two input datasets. The position score is the rank average in each dataset as defined by a value ranging between -1 and 1. For the analysis we ranked the genes for each dataset based on the  $\log_2$  fold change values.

In order to estimate a similarity score between two datasets, we estimated the Spearman correlation coefficient between the position scores for the significant gene sets with  $FDR \leq 0.05$ . The analyses were conducted both separately for GO-terms and CPDB-pathways, as well as combined. [Figures 3H](#), [S4A](#), and [S5A–S5C](#) indicate the scores of commonly significant GO-terms and CPDB-pathways between drug-persistent 3-D organoids vs. vehicle-control counterparts (plotted in the Y axis) and diapause or normal embryonic stages vs. E4.5 epiblast ([Boroviak et al., 2015](#)) plotted on the X axis. The Spearman correlation coefficient is indicated in each Figure.

### Gene Essentiality Data

CERES scores ([Meyers et al., 2017](#)) as metrics of gene essentiality in conventional 2D cultures, were examined for various genes commonly upregulated/downregulated across different drug-persistent PDO and PDX models based on results from genome-scale *in vitro* CRISPR/Cas9 gene knockout screens of the Dependency Map program ([www.depmap.org](http://www.depmap.org)) performed with the AVANA sgRNA library. The patterns of essentiality for different genes of interest were consistent across several different releases of data from the Dependency Map studies.

### QUANTIFICATION AND STATISTICAL ANALYSIS

Cell viability data are expressed as means with the standard error of the mean (SEM). When applicable, comparisons between groups was performed using two-way ANOVA test (see figure legends). The Spearman correlation coefficient was used to assess statistical significance in correlative analyses. Survival data were plotted as Kaplan-Meier survival curves and log-rank test was used to determine statistical significance. The p values  $\leq 0.05$  were considered significant. Data were analyzed using GraphPad Prism software (Graphpad, V8.0 and V9.0)

## Supplemental Information

### **An Embryonic Diapause-like Adaptation with Suppressed Myc Activity Enables Tumor Treatment Persistence**

**Eugen Dhimolea, Ricardo de Matos Simoes, Dhvanir Kansara, Aziz Al'Khafaji, Juliette Bouyssou, Xiang Weng, Shruti Sharma, Joseline Raja, Pallavi Awate, Ryosuke Shirasaki, Huihui Tang, Brian J. Glassner, Zhiyi Liu, Dong Gao, Jordan Bryan, Samantha Bender, Jennifer Roth, Michal Scheffer, Rinath Jeselsohn, Nathanael S. Gray, Irene Georgakoudi, Francisca Vazquez, Aviad Tsherniak, Yu Chen, Alana Welm, Cihangir Duy, Ari Melnick, Boris Bartholdy, Myles Brown, Aedin C. Culhane, and Constantine S. Mitsiades**

Figure S1: Three-dimensional cancer organoid models

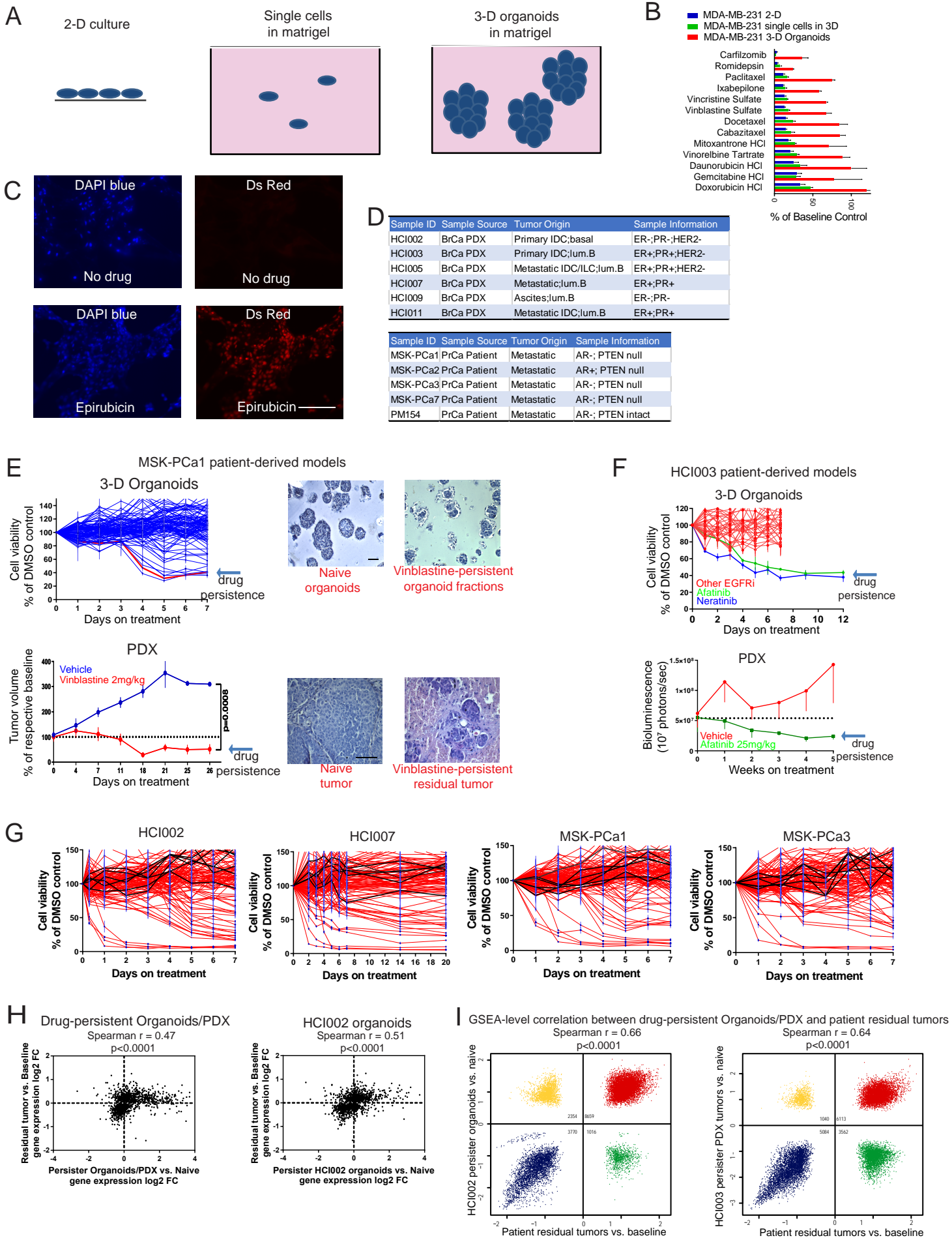


**Figure S1. Three-dimensional cancer organoid models, related to Figure 1.**

(A) Schematic representation of the three types of cell culture models (see Methods) used in the experiment of panel B: 1) conventional 2-D culture in flat plastic surface, 2) cells in 3-D gels before the formation of organoids (single-cell format), 3) fully-formed 3-D organoids in matrigel.

(B) Viability of MDAMB-231 cells after treatment (72h, 100nM) with common chemotherapeutic agents (selected drug examples from larger chemical screens [Dhimolea *et al.*, in preparation] are shown) in the three *in vitro* culture systems described in Panel A. Most active compounds had markedly reduced efficacy against 3-D organoids in short-term assays compared to respective 2-D cultures, or to single-cell gels, indicating that gel matrix properties cannot account for the reduced chemotherapeutic cytotoxicity in 3-D organoids (quadruplicates; mean  $\pm$  SEM).

(C) Representative example of fluorescence-based imaging of sections from MDAMB-231 organoid cultures after 12h exposure to epirubicin (100nM), indicating the drug molecule can readily penetrate the interior of 3-D organoids (also see Methods); scale bar 50  $\mu$ m.

(D) Characteristics of BrCa and PrCa patient-derived models established as 3D-organoids (PDO) *in vitro* or as PDXs *in vivo* in this study. Abbreviations denote histological/molecular subtypes: invasive ductal carcinoma (IDC), invasive lobular carcinoma (ILC), and luminal B (LumB).

(E) Longitudinal response of MSK-PCa1 PDO (quadruplicates; mean  $\pm$  SEM) to the compounds of the FDA-approved oncology drugs panel (upper left; 100nM; each line corresponds to one drug; vinblastine highlighted with red) and validation in the respective PDX model (lower left) as well as *in vitro* (upper) and *in vivo* (lower) histological similarities with evidence of cancer cell killing or necrotic tissue around the drug-persistent residual foci; H&E staining; scale bar 50  $\mu$ m.

(F) Time-lapse response of HCI003 PDO (quadruplicates; mean  $\pm$  SEM) to 33 EGFR inhibitors segued by persistence (longitudinal curve plateauing) to afatinib and neratinib during prolonged exposure (top) and validation of afatinib response in respective PDX (bottom).

(G) Representative examples of time-lapse response of several PDO models (quadruplicates; mean  $\pm$  SEM) to the FDA-Approved Oncology Set drug panel (100nM). Each red curve represents the longitudinal response to one drug (black curves indicate DMSO controls); notice the plateauing of the curves with some drugs after the initial reduction of cell viability, indicating adapted drug-persistent cell population (TP-organoid fractions).

(H) Scatter plots comparing for individual genes the aggregate gene expression changes in residual tumors of BrCa patients (Kimbung *et al.*, 2018) after 2 neoadjuvant chemotherapy cycles vs. baseline (genes with significant changes [FDR<0.05] shown; dataset GSE87455, see Methods) vs. 1) with those of our drug-persistent BrCa/PrCa preclinical models of residual disease vs. respective vehicles (aggregate expression changes in 8 TP-organoid and 2 PDX residual tumor models; treated with docetaxel, afatinib or vinblastine) (*left*) and 2) with those in TNBC docetaxel-persister HCI002 organoids (*right*), shown as individual example.

(I) Scatter-plot showing gene set enrichment scores (encompassing CPDB and GO terms) in residual tumors of BrCa patients (Kimbung *et al.*, 2018) after 2 neoadjuvant chemotherapy cycles vs. baseline (aggregate enrichment; dataset GSE87455, see Methods) vs. enrichment scores in examples of drug-persistent organoid (*left*) or PDX (*right*) fractions vs. respective vehicles.

Figure S2: Treatment-persistent organoid (TP-organoid) models

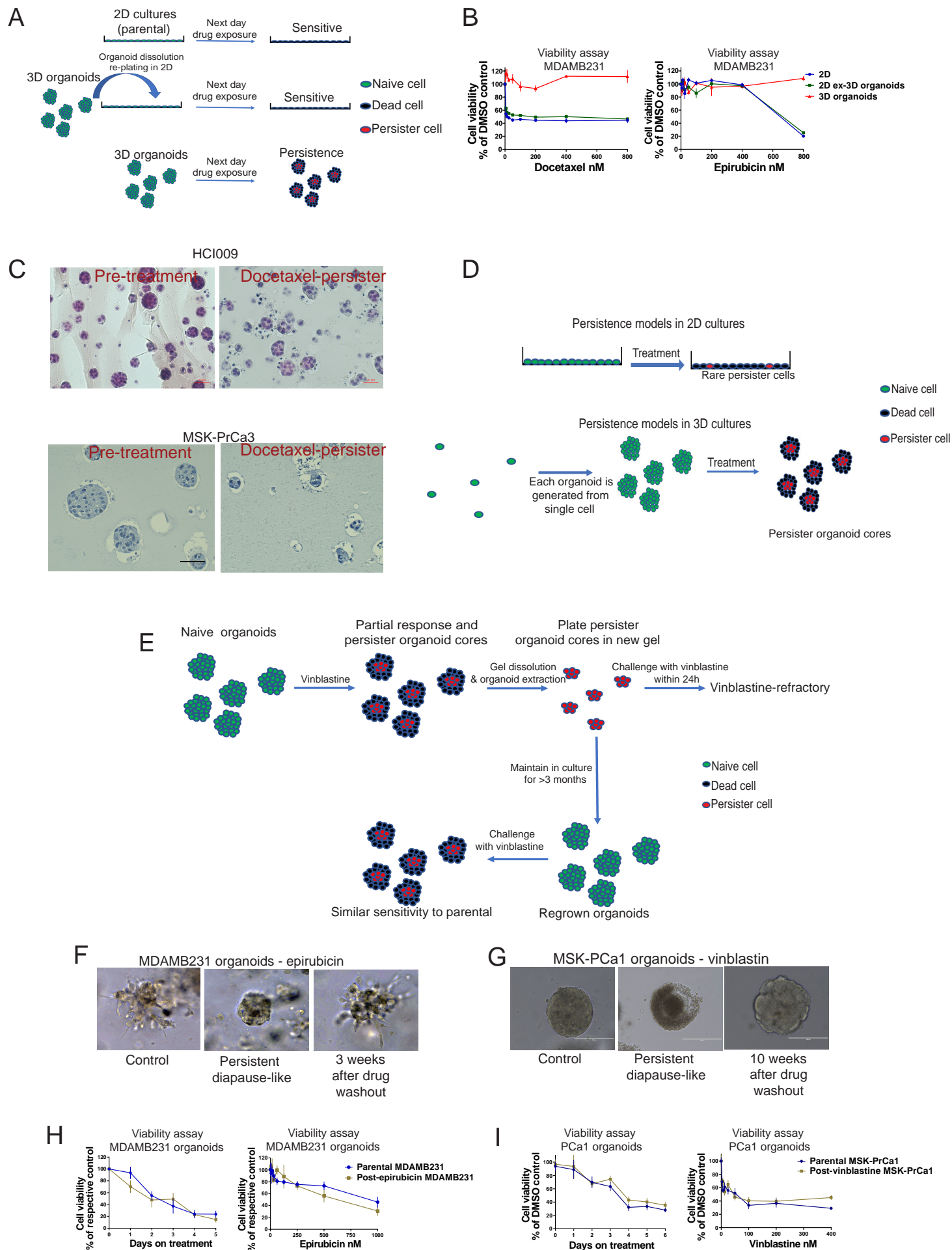


**Figure S2. Treatment-persistent organoid (TP-organoid) models, related to Figure 1.**

(A and B) Schematic representation of experiment (A) and response of MDAMB-231 parental cells in 2-D cultures, cells extracted from organoids and re-plated in 2D culture (2D ex-3D organoids), and 3-D organoids to docetaxel (24h) and epirubicin (48h) treatment (B); quadruplicates; mean  $\pm$  SEM.

(C) Treatment-naïve and docetaxel-persister organoid cores (similar to those in Figures 1B and 1D) of two additional PDO models (quadruplicates; mean  $\pm$  SEM); H&E staining; scale bar 50  $\mu$ m.

(D) Schematic representation of the distinct phenotypic features of drug-persistence in 2-D cultures and 3-D cultures: each organoid originates from a single cell and, upon treatment, generates a drug-persistent fraction.

(E) Schematic representation of the experimental workflow for experiments in panels F-I.

(F) MDAMB-231 organoid treated with DMSO (*left*); epirubicin-persister organoid fractions (after 4 days continuous drug treatment; 500 nM) re-cast in a new gel (*middle*); regrowth of persister organoid fractions ~3-4 weeks after epirubicin washout (*right*).

(G) PrCa organoid treated with DMSO (*left*); vinblastine-persister (*middle*) organoid fractions (generated after 10 days continuous drug treatment, 100nM; notice cell death debris around residual viable organoid); regrowth of persister organoid fractions 10-12 weeks after vinblastine washout (*right*).

(H and I) Drug sensitivity of MDAMB-231 (H) and MSK-PCa1 (I) parental organoids vs. organoids re-grown from treatment-persister cores (shown in F and G) after washout (quadruplicates; mean  $\pm$  SEM); time-lapse responses to 1 $\mu$ M of chemotherapeutic and dose-responses after 72h drug exposure are shown.

# Figure S3: Suppression of Myc activity induces diapause-like dormant molecular adaptation in cancer cells

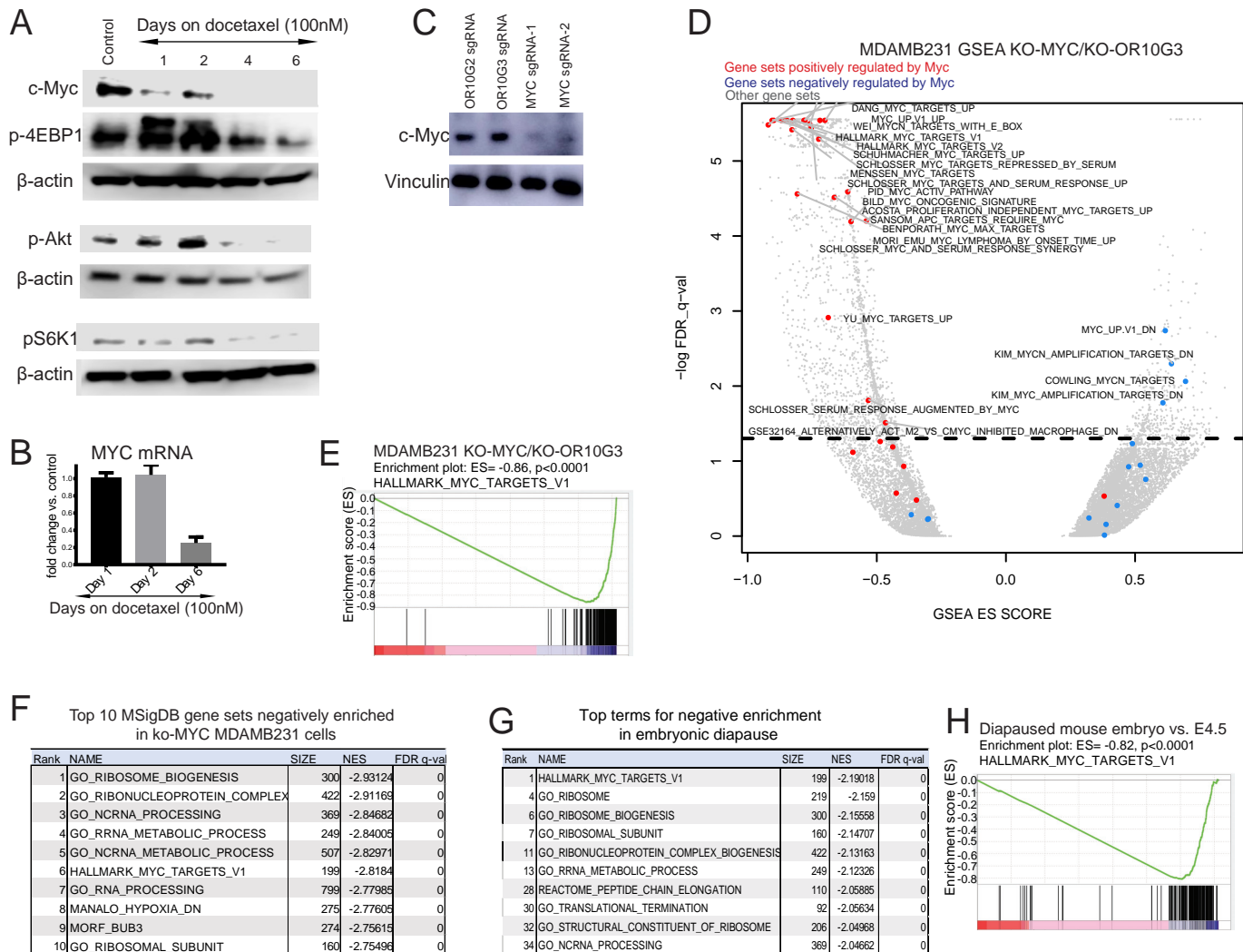


**Figure S3. Suppression of Myc activity induces diapause-like dormant molecular adaptation in cancer cells, related to Figure 3.**

(A) Western blot analyses showing protein level changes during treatment of MDAMB-231 organoids with docetaxel (100nM).

(B) *MYC* transcript level changes from RNA sequencing data during treatment of MDAMB-231 organoids with docetaxel (100nM).

(C-E) Validation of CRISPR-Cas9 mediated Myc protein down-regulation in MDAMB-231 cells by western blot (CRISPR-Cas9 mediated KO of olfactory receptor genes *OR10G2* and *OR10G3* are used as controls) (C); analysis of MSigDB gene sets positively (red) or negatively (blue) regulated by Myc (D); and gene set enrichment plot for a selected example of Myc-driven gene set (FDR<0.001) (E).

(F) Top gene sets negatively enriched in *MYC*-KO MDAMB-231 cells (analysis using MsigDB compendium, 17810 gene sets in total).

(G and H) Top gene sets negatively enriched in diapaused mouse embryos (Boroviak et al., 2015) (G, analysis using the MsigDB compendium, 17810 gene sets in total) and gene set enrichment plot for a selected example of Myc-driven gene set (H).

Figure S4: The transcriptional adaptation in TP-organoids resembles embryonic diapause

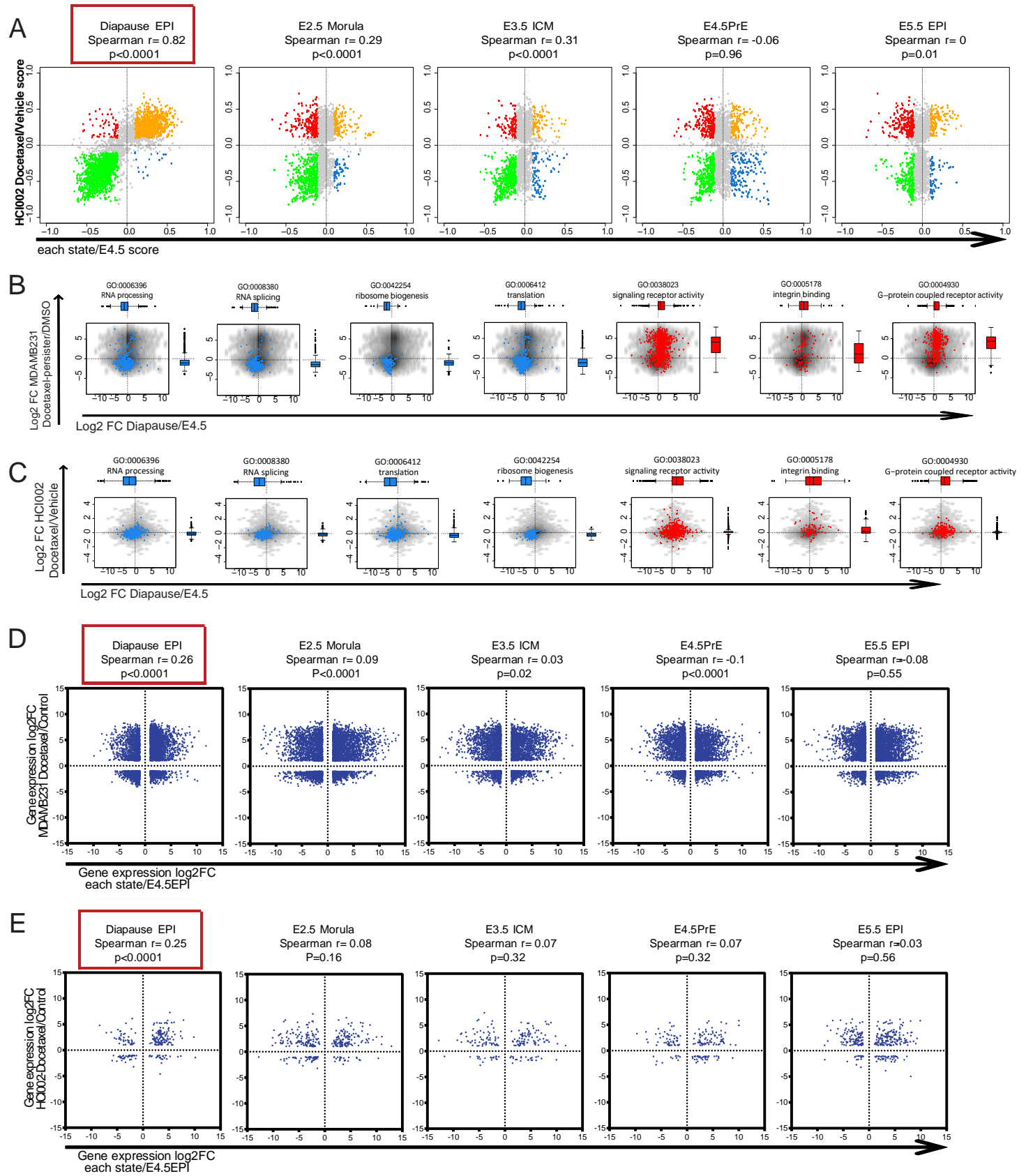


**Figure S4. The transcriptional adaptation in TP-organoids resembles embryonic diapause, related to Figure 3.**

(A) 2D GO enrichment comparisons (similar to Figure 3H; including CPDB pathways and GO terms; see Methods) between docetaxel-persistent HCI002 BrCa PDOs vs. different mouse embryo developmental stages (Boroviak dataset (Boroviak et al., 2015)). Spearman correlation coefficients indicate pronounced similarity of the docetaxel-persistent 3-D organoids to the diapaused E4.5 epiblast but not to other embryonic stages [comparisons similar to those performed by (Bulut-Karslioglu et al., 2016) and (Scognamiglio et al., 2016)].

(B and C) Scatterplots and box plots of previously-described (Scognamiglio et al., 2016) hallmark GO terms of embryonic diapause which exhibit significant changes (FDR<0.05) both in the comparison between mouse embryonic diapause vs. E4.5 epiblasts and in the comparison of chemo-persistent vs. control organoids in our 3-D cultures of MDAMB-231 (B) and HCI002 (C) cells. Gray dots represent all genes. Blue and red dots represent genes of downregulated and upregulated pathways, respectively.

(D and E) Comparisons of gene-level transcriptional changes [analyses similar to those performed using *in vitro* models of embryonic diapause by (Bulut-Karslioglu et al., 2016)] between different mouse developmental stages vs. docetaxel-persistent MDAMB-231 organoids (D, genes with FC>1 in both settings included) or vs. docetaxel-persistent HCI002 PDOs (E, genes with FC>1 and FDR<0.1 in both datasets included). Spearman correlation coefficient indicates significant gene-level correlation between transcriptional changes in docetaxel-refractory organoids and mouse diapaused E4.5 epiblast (but not to other embryonic stages), with score values similar or higher to those reported in studies of syngeneic *in vitro/in vivo* mouse diapause models (Scognamiglio et al., 2016, Bulut-Karslioglu et al., 2016).

Figure S5: The transcriptional adaptation in treatment-persistent tumors cells of preclinical models and patients resembles embryonic diapause

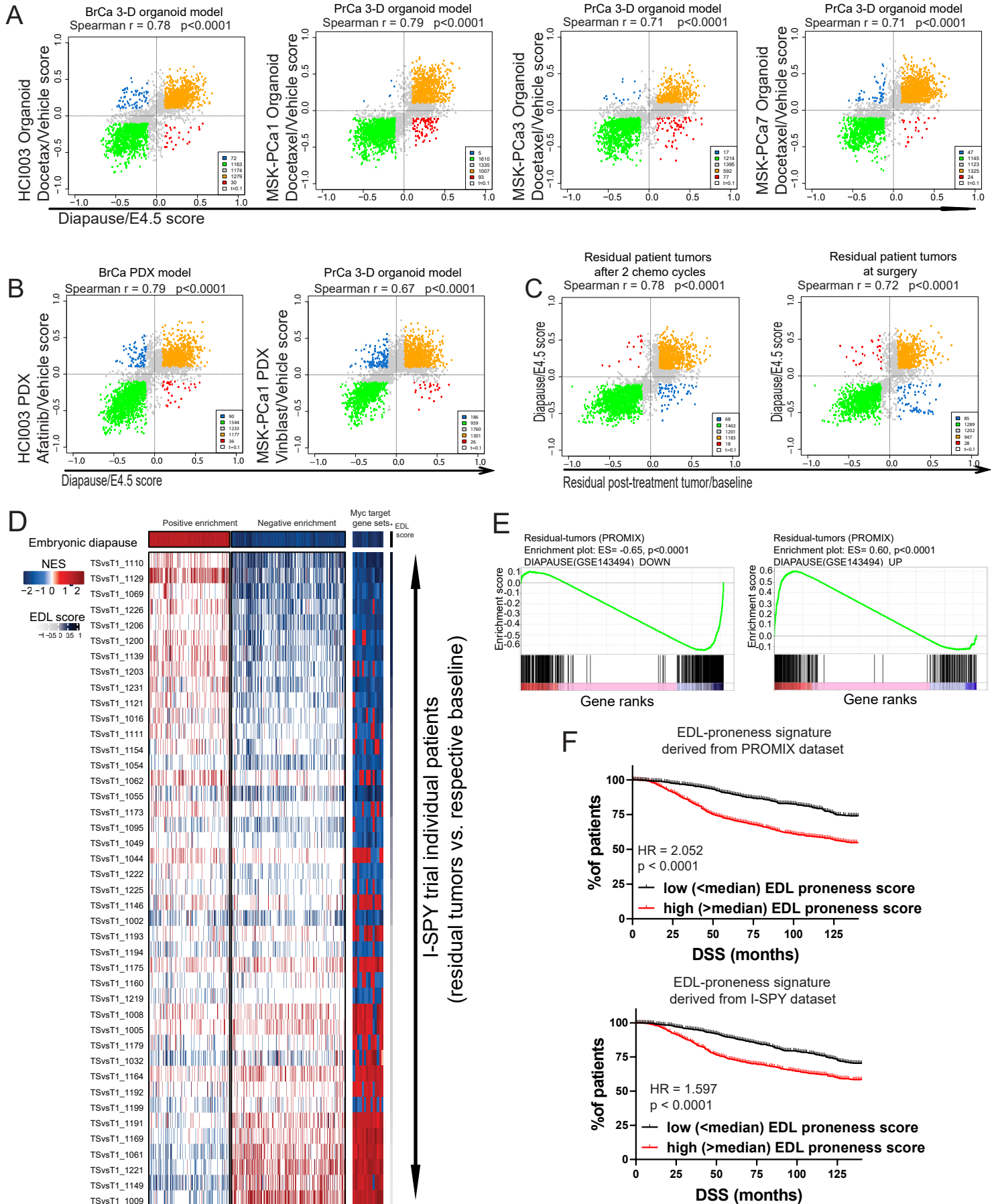


**Figure S5. The transcriptional adaptation in treatment-persistent tumors cells of preclinical models and patients resembles embryonic diapause, related to Figure 3.**

(A-C) 2D-GO gene set analysis (encompassing CPDB pathways and GO terms; see Methods) comparing the transcriptional changes in several BrCa and PrCa drug-persistent PDO models (A), post-treatment residual PDX tumors (B) and post-treatment residual tumors in BrCa patients [dataset GSE87455 from (Kimbung et al., 2018); aggregate patient samples are shown] after 2 chemotherapy cycles or at surgery (C), with the transcriptional changes in the diapaused E4.5 epiblast.

(D) Heatmap depicting the MSigDB gene sets significantly enriched in embryonic diapause and their respective enrichment status in post-neoadjuvant chemotherapy residual tumor fractions in individual patients of the I-SPY trial [dataset GSE32603 (Magbanua et al., 2015)]; notice the association between the embryonic diapause-like (EDL) score (as metric of molecular signature correlation with embryonic diapause; see Methods) and the enrichment status of Myc target gene sets (14 gene sets with significant negative enrichment in either embryonic diapause or the clinical dataset are shown).

(E) Representative gene set enrichment plots in the post-neoadjuvant chemotherapy residual tumors of PROMIX trial patients (aggregate expression) for the gene signatures down-regulated or upregulated in the embryonic diapause dataset GSE143494. This comparison was performed to further confirm the similarities between the transcriptional signatures of embryonic diapause and chemo-persister residual tumor cells (in preclinical models and patients) using another (different from the Boroviak *et al.* study) experimental dataset of diapaused mouse embryos.

(F) Disease-specific survival (DSS) of METABRIC patients stratified by their EDL-proneness signature [independently derived from either the PROMIX (Kimbung et al., 2018) or the I-SPY (Magbanua et al., 2015) trials datasets; see Methods] is inferior in patients whose baseline tumors exhibited higher EDL-proneness signature (i.e. patients whose pre-treatment BrCa had higher probability to develop treatment-persistence through diapause-like adaptation; see Methods). This analysis was necessitated by the absence from the METABRIC dataset (or other studies of similar size) of molecularly characterized samples from treatment-persistent residual disease.

**Figure S6: Suppression of Myc activity induces diapause-like molecular changes and attenuates the cytotoxic effect of chemotherapeutic drugs in cancer cells**

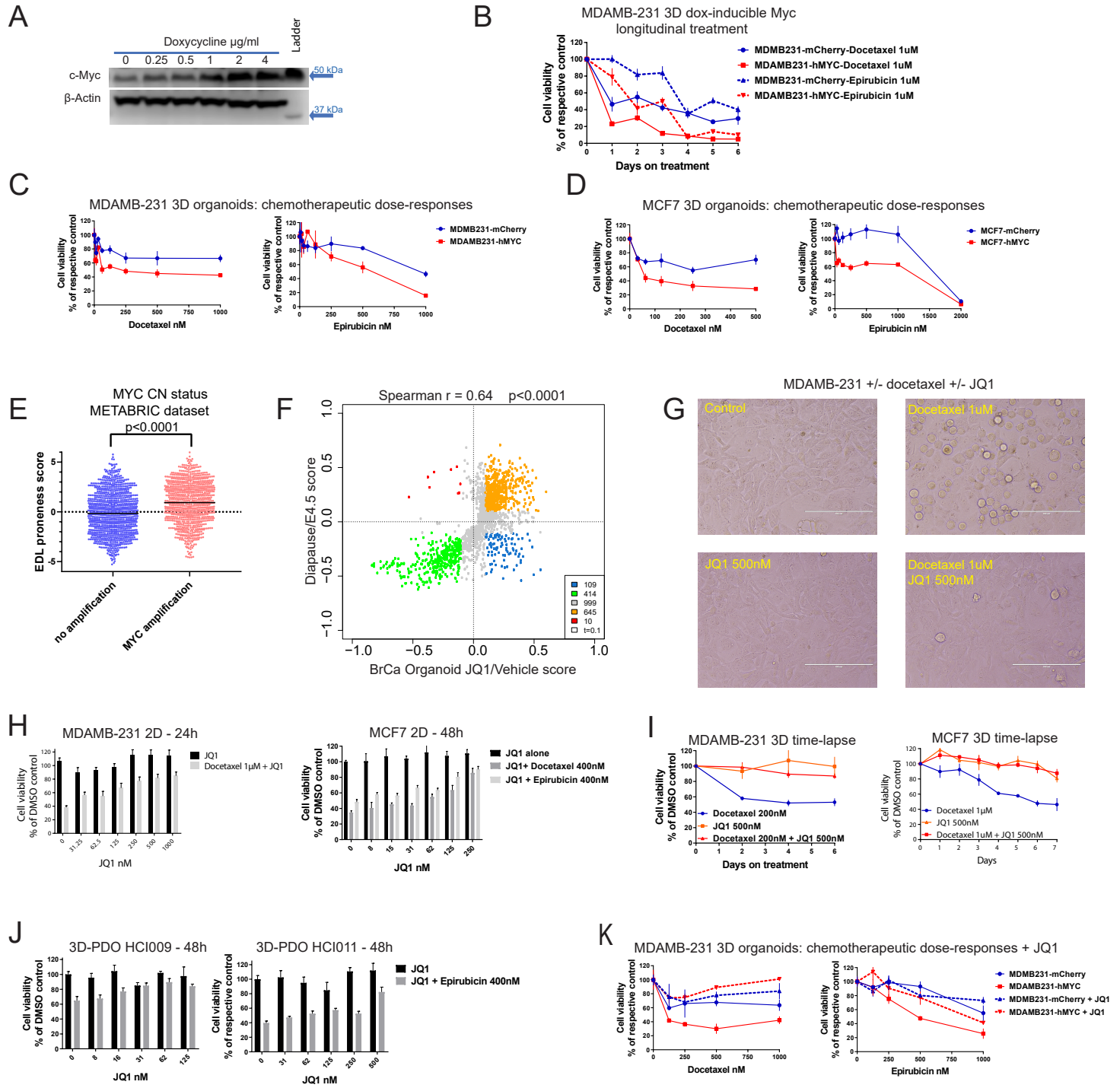


**Figure S6. Suppression of Myc activity induces diapause-like molecular changes and attenuates the cytotoxic effect of chemotherapeutic drugs in cancer cells, related to Figure 4.**

(A) Western blot confirming doxycycline-inducible expression of Myc in MDAMB-231 cells.

(B) Longitudinal effect of chemotherapeutics on MDAMB-231 organoids expressing doxycycline-inducible c-Myc or mCherry (as control);  $p < 0.0001$  for both drugs, two-way ANOVA with Sidak test for correction of multiple comparisons for different time-points.

(C-D) Response of MDAMB-231 (C) and MCF7 (D) 3-D organoids (quadruplicates; mean  $\pm$  SEM), exogenously expressing doxycycline-induced Myc, or mCherry (as control), to chemotherapeutic agents (5 and 7 days time points, respectively);  $p < 0.0001$ , two-way ANOVA with Sidak test for correction of multiple comparisons for different doses.

(E) EDL-proneness scores of baseline BrCa tumors with vs. without *MYC* amplification in the METABRIC dataset.

(F) Longitudinal treatment of organoids with JQ1 (500nM) induces transcriptional changes similar to the changes observed in embryonic diapause (vs. treatment-naïve counterparts); 2D-GO enrichment comparison.

(G) Phase contrast microscopy of MDAMB-231 cells exposed to docetaxel in the presence or absence of JQ1; 24h; scale bar 200  $\mu$ m.

(H-J) JQ1 attenuated the cytotoxic effect of chemotherapeutics in 2-D (H) and 3-D cultures (I) of breast cancer cell lines and in PDO models (J); quadruplicates; mean  $\pm$  SEM.

(K) Doxycycline-inducible Myc-mediated chemo-sensitization of BrCa 3-D organoids (quadruplicates; mean  $\pm$  SEM) is attenuated by JQ1 (4 day time point;  $p < 0.0001$  for docetaxel and  $p = 0.009$  for epirubicin, two-way ANOVA for viability with Sidak test for correction of multiple comparisons for different doses.

Figure S7: The EDL adaptation in cancer cells has distinct phenotypic and molecular features

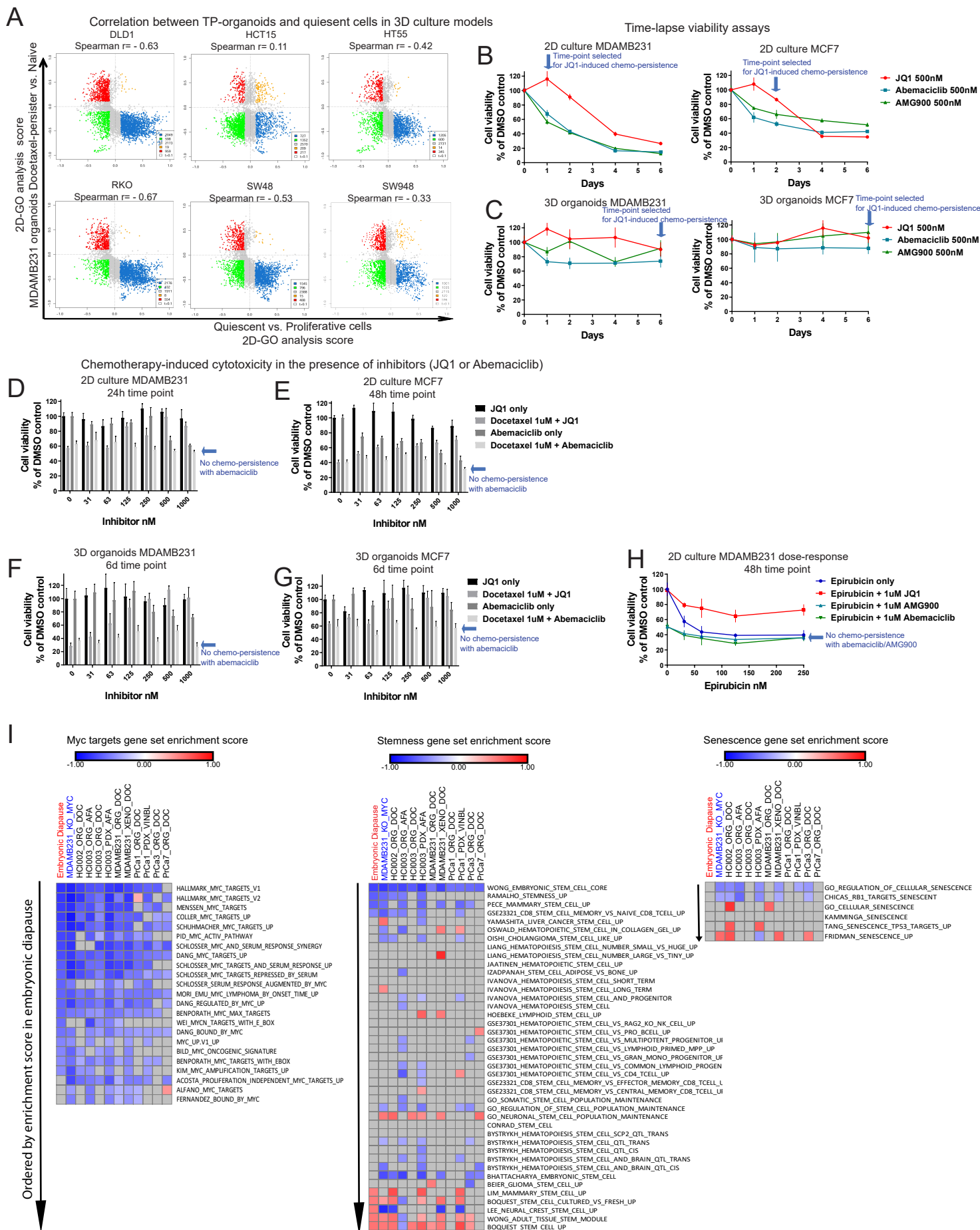


**Figure S7. The EDL adaptation in cancer cells has distinct phenotypic and molecular features, related to Figure 6.**

(A) 2D-GO enrichment comparison (see Methods) of transcriptional changes between Docetaxel-persistent\_vs\_Treatment-naive MDAMB-231 organoids and Quiescent\_vs\_Proliferative cells from six different colon cancer organoid models from public dataset GSE114012; orange/green = concordantly upregulated/downregulated; red/blue = anti-correlated changes; gray = below 0.1 threshold score.

(B-C) Time-lapse response of 2-D cultured cell lines (B) and respective 3-D organoids (C) exposed to JQ1, abemaciclib and AMG900. Each curve represents the longitudinal response to one compound. Time-points selected for JQ1-induced chemo-refractoriness assays (panels D-H) in each culture setting are indicated by arrows; quadruplicates; mean  $\pm$  SEM.

(D-H) An independent set of experiments showing co-treatment of 2-D cultures (D-E) or 3-D organoids (F-G) of MDAMB-231 (D, F) or MCF7 (E, G) human BrCa cell lines with docetaxel (D-G) or epirubicin (H) with JQ1, Abemaciclib or AMG900. Cell cycle inhibitors do not phenocopy the effect of JQ1 on conferring attenuation of cytotoxicity (quadruplicates; mean  $\pm$  SEM)

(I) Enrichment scores for gene sets of the MsigDB compendium related to Myc transcriptional output, stemness and senescence in the mouse diapaused embryos, MDAMB-231 *MYC*-KO cells, and the diapause-like treatment-persister organoids and PDX models (treated with docetaxel, vinblastine or afatinib), ordered vertically according to enrichment score in embryonic diapause; non-significant ( $p > 0.05$ ) enrichment scores shown in gray.

Figure S8: The diapause-like persister tumor cell adaptation is distinct and reversible

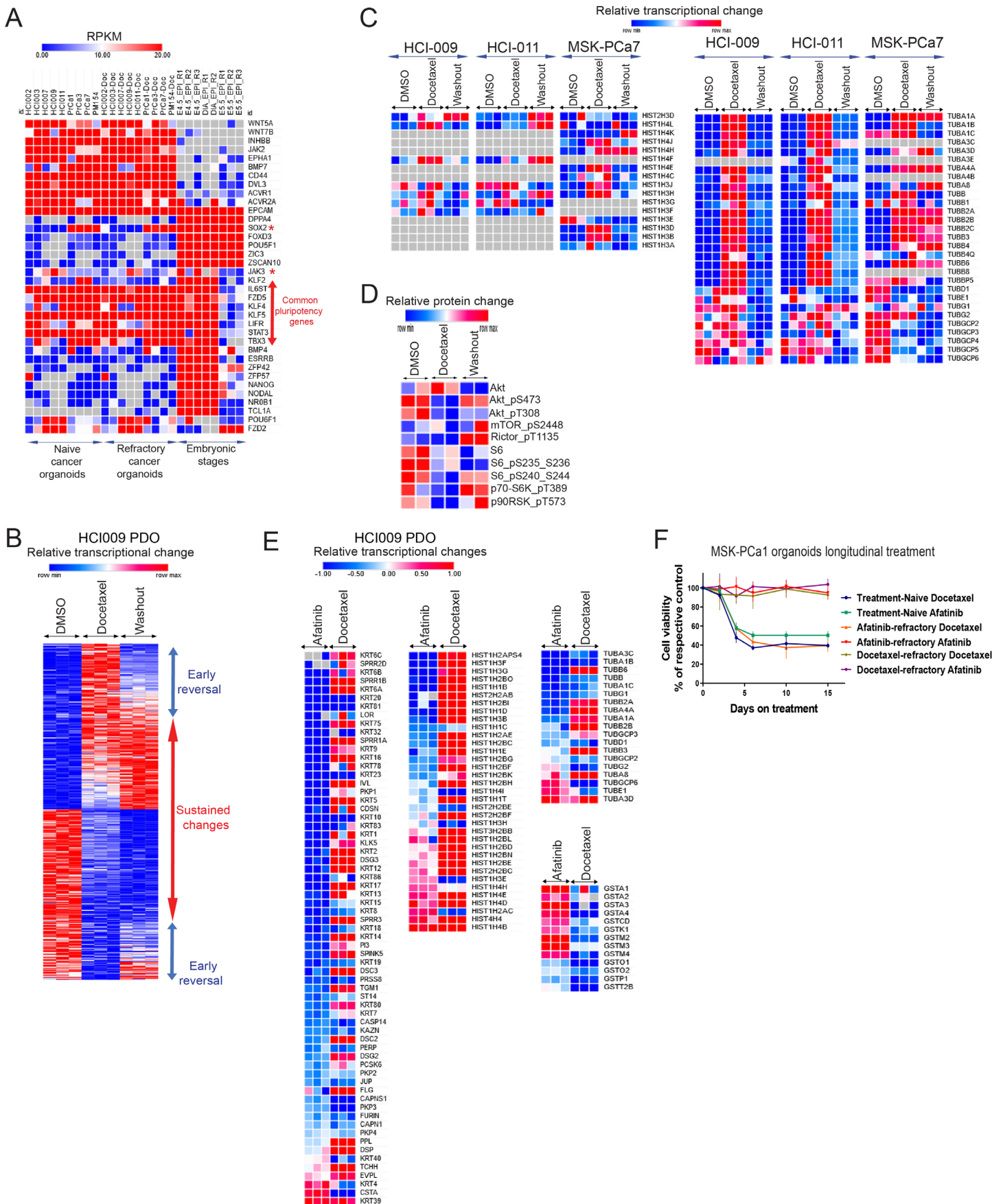


**Figure S8. The diapause-like persister tumor cell adaptation is distinct and reversible, related to Figure 6.**

(A) Normalized expression of general pluripotency genes in control and docetaxel-persister (Doc) EDL organoids, and in mouse epiblast stages day-4.5, diapause (DIA), and day-5.5 (Boroviak et al., 2015).

(B) Relative expression of significantly ( $FDR < 0.05$ ) altered transcripts in organoids, during docetaxel treatment and 3 days after docetaxel washout. The figure shows experimental triplicates.

(C) Transcriptional changes in histone and tubulin gene families in docetaxel-persistent organoids and 3 days after docetaxel washout in PDO models; normalized counts; experimental triplicates.

(D) Proteomic (RPPA; see Methods) changes in ribosomal biosynthetic activity in docetaxel-persistent organoids and 3 days after drug washout in HCI009 PDO, compared to the average of respective controls (experimental duplicates); concordant with proteomic biosynthetic markers in mouse embryonic diapause (Bulut-Karslioglu et al., 2016).

(E) Examples of gene families (histones, keratins, tubulins, glutathione S-transferases) expression changes in afatinib-persistent and docetaxel-persistent PDOs (each drug condition compared to DMSO-treated control).

(F) Naïve MSK-PCa1 organoids and afatinib-persistent or vinblastine-persistent organoid fractions (as shown in Suppl. Figures S1D and S2G) were extracted from the gel, recast in new gels and longitudinally re-exposed to afatinib and vinblastine (100nM). Notice cross-resistance in vinblastine-refractory organoids and lack thereof in afatinib-refractory organoids (quadruplicates; mean  $\pm$  SEM). Further results obtained after drug-washout and followed by prolonged (~3 months) re-growth cultures of these persistent organoid cores are shown in Suppl. Figure S11.

Figure S9: Diapause-like persister organoids have distinct therapeutic vulnerabilities

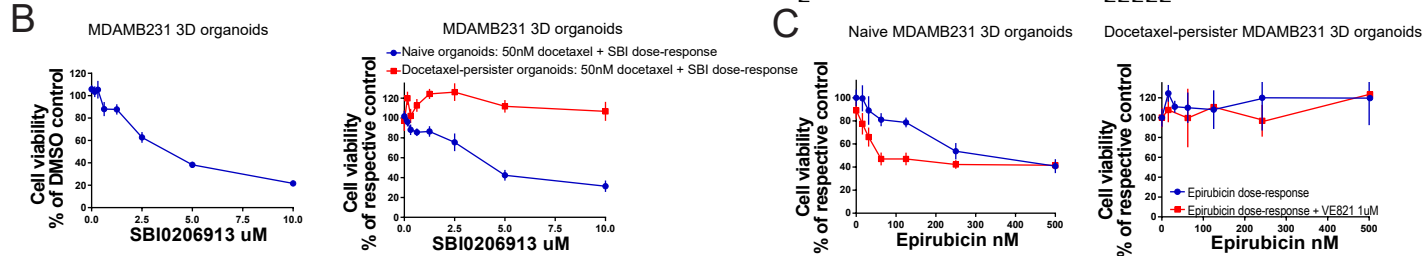
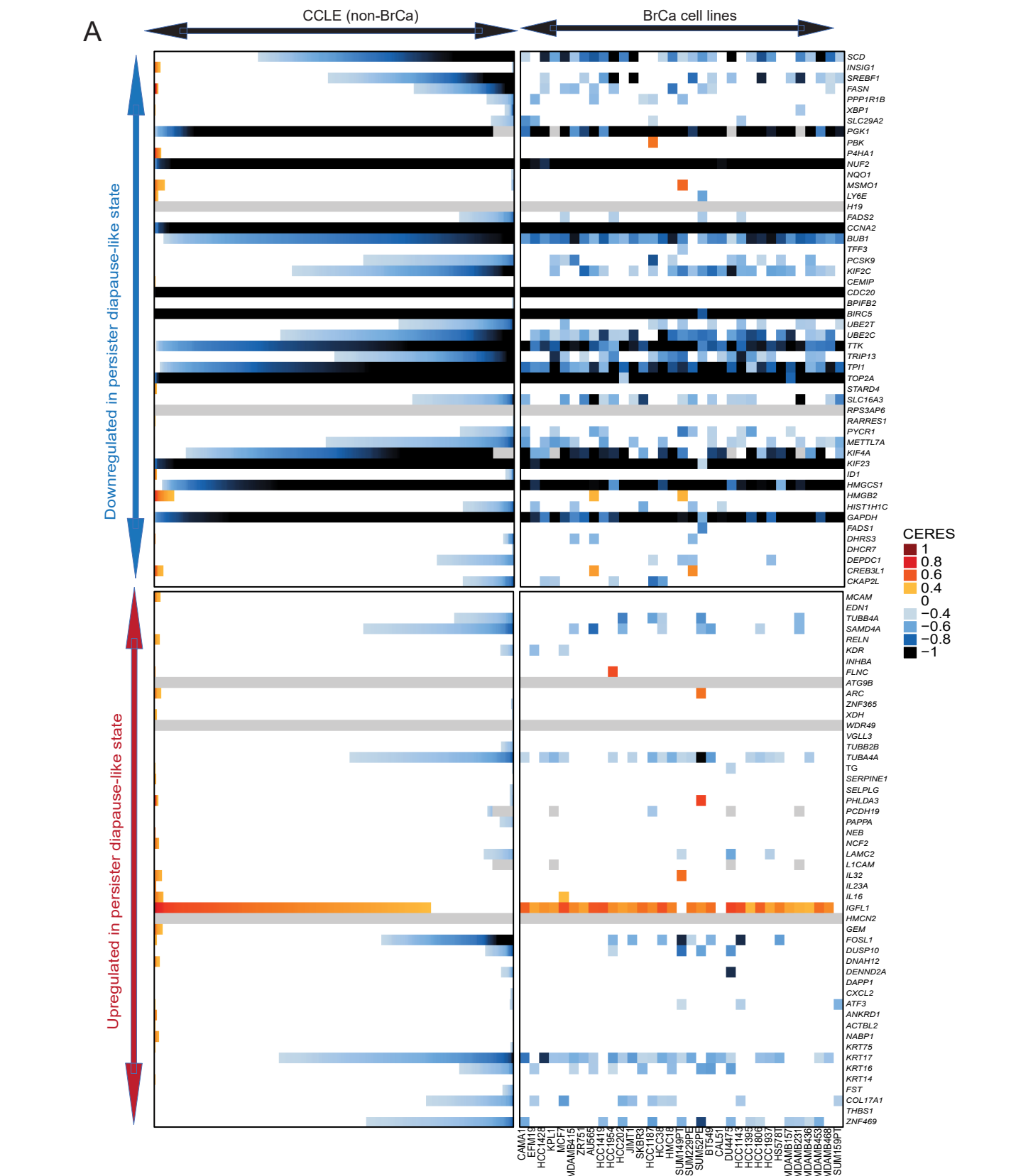


**Figure S9. Diapause-like persister organoids have distinct therapeutic vulnerabilities, related to Figure 7.**

(A) CERES scores for essentiality of the top 100 genes commonly upregulated/downregulated across 9 drug-persistent PDO and PDX models. CERES scores, derived from CRISPR-based genome-scale knockout screens conducted in 2D *in vitro* cultures by the Dependencies Map program, Broad Institute (Meyers et al., 2017)), are depicted for breast cancer cell lines as a matrix (right side of graph) of cell lines (in columns) and genes (in rows); while data for non-breast lines are depicted for each gene (row) as stacked bars, to visualize CERES scores in descending order (from left to right) for each gene. Black or dark blue color indicates negative CERES scores, compatible with pronounced sgRNA depletion in a given cell line; conversely red indicates enriched sgRNAs for the respective genes.

(B) Response of treatment-naïve MDAMB-231 organoids (quadruplicates; mean  $\pm$  SEM) to autophagy inhibitor SBI0206913 (left) and effect of the combination of docetaxel (50nM) and SBI0206913 dose-response (5 days exposure) on the viability of naïve MDAMB-231 organoids (simultaneously co-treated with both compounds), and of treatment-persister organoids (pre-treated for 1 week with 50nM docetaxel to establish persister cells) (right). Dose-response curves of combined docetaxel and SBI0206913 treatments (right) were normalized to their respective docetaxel-containing and SBI0206913-free control, to directly visualize the differential effect of SBI0206913 on docetaxel sensitivity of naïve versus docetaxel-persister organoids.

(C) Effect of epirubicin, in the presence vs. absence of ATR inhibitor VE821, on the viability of treatment-naïve MDAMB-231 organoids (simultaneously co-treated with both compounds), and of docetaxel-persister organoids (pre-treated for 1 week with docetaxel to establish persister cells); 5 days drug exposure; quadruplicates; mean  $\pm$  SEM.